Time reversal beamforming to ultrasonic implants using a custom phased array

by

Braeden Christopher Benedict

A thesis submitted in partial satisfaction of the

requirements for the degree of

Joint Master of Science
with the University of California, San Francisco

in

Bioengineering

in the

Graduate Division

of the

University of California, Berkeley

Committee in charge:

Professor Rikky Muller, Chair
Professor Steven Conolly
Professor Chris Diederich

Summer 2021

Time reversal beamforming to ultrasonic implants using a custom phased array

Abstract

Time reversal beamforming to ultrasonic implants using a custom phased array

by

Braeden Christopher Benedict

Master of Science in Bioengineering

University of California, Berkeley

Professor Rikky Muller, Chair

Millimeter-scale implants using ultrasound for power and communication have been proposed for a range of deep-tissue applications, including neural recording and stimulation. However, published implementations have shown high sensitivity to misalignment with the external ultrasound transducer. Ultrasonic beamforming using a phased array to these implants can improve tolerance to misalignment, reduce implant volume, and allow multiple implants to be operated simultaneously in different locations.

This report details the design of a custom planar phased array ultrasound system, which is capable of steering and focusing ultrasound power within a 3D volume. Analysis and simulation is performed to determine the choice of array element pitch, with special attention given to maximizing the power available at the implant while meeting FDA limits for diagnostic ultrasound. The design of the ultrasound system is described, with a particular emphasis on signal integrity and noise minimization.

Time reversal is proposed as a computationally simple approach to beamforming that is robust despite scattering and inhomogeneity of the acoustic medium. This technique is demonstrated both in active drive and pulse-echo modes, and it is experimentally compared with other beamforming techniques by measuring energy transfer efficiency at varying depths and angles. Simultaneous power delivery to multiple implants is also demonstrated.

Table of Contents

List of Figures

List of Tables

Acknowledgments

I would first like to thank all my family and friends who have supported me throughout my studies. I thank Nathan Ersumo for his help with piezo dicing and mentorship as my fellow Bioengineering student in the group. I also would like to thank Sina Faraji Alamouti, Dr. Soner Sonmezoglu, and Prof. Chris Diederich for technical discussions. I am grateful to Prof. Steven Conolly for his career guidance and serving on my thesis committee. I owe many thanks to Mohammad Meraj Ghanbari, who initially began this work and has served as a mentor for me these past two years. Finally, I would like to thank my advisor Prof. Rikky Muller for her mentorship and support.

Portions of this report were adapted from [1], a conference proceeding covering part of this work.

Chapter 1

Introduction

1.1 Ultrasonic implants
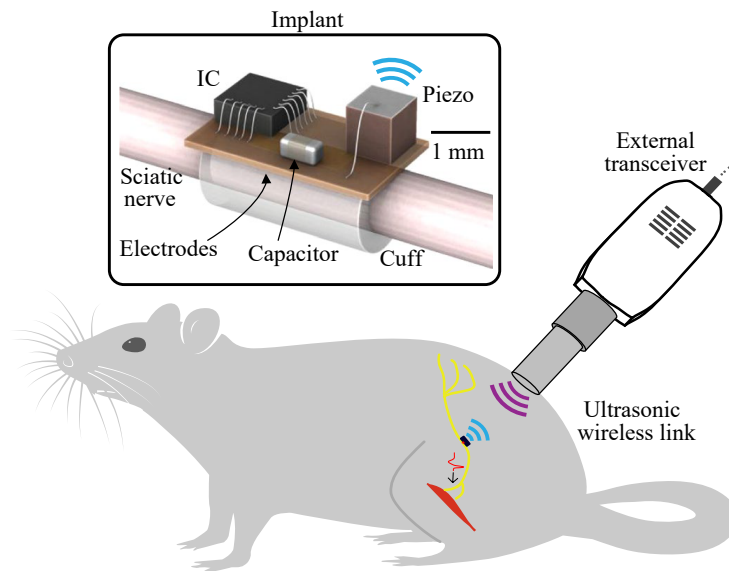
Figure 1.1: Example of neural stimulator system with diagram of ultrasonic implant. Adapted with permission from [2].

Wireless millimeter-scale implants are attractive due to their minimal invasiveness and untethered operation, and they have been proposed for a range of peripheral nerve recording and stimulation applications [2], [3]. Ultrasound (US) has emerged as a promising power delivery and communication modality for deep-tissue implants. When compared with electromagnetic waves, US offers efficient propagation in tissue and a relatively small wavelength, which enable the use of millimeter and sub-millimeter scale acoustic resonators implanted

in deep tissue [2], [4]. Such an US implant includes a piezoceramic resonator (piezo), an integrated circuit (IC), and optionally an energy storage capacitor. An external transducer provides US energy which is received by the piezo and rectified by the IC. The implant communicates with the external transducer (which also functions as a receiver) either by actively driving its piezo [5] or through passive backscattering [6]. A diagram of such a system, including the implant and external transducer, is shown in Fig. 1.1 [2]. In the latter case, modulation of the impedance across the piezo terminals changes the reflection coefficient at the piezo and modulates the amplitude of the reflected ultrasound [7]. Piezo volume is a large portion of the total implant volume and determines the harvestable power for a given US intensity [7]. Therefore, greater intensity at the implant allows for a reduction of implant volume.

A single-element focused or unfocused external transducer is used with most published US implants. A focused transducer provides greater link efficiency for high power applications such as neural stimulation, but this setup can tolerate only a few millimeters misalignment [2], [3]. An unfocused transducer is generally less sensitive to misalignment, but it still has a natural focal length given by its diameter and wavelength. Before this distance, termed the near-field region, there are local minima and maxima which are dependent on the medium and difficult to predict [8]. Thus, implants are typically placed beyond this focal point in the far-field, which provides yet another constraint for this single-transducer setup. While multiple implants could be powered using a single transducer if placed in close proximity to one another, it is preferable to record or stimulate at multiple locations.

1.2 Phased array beamforming

To overcome the limitations of a single external transducer, a transducer array can be used to dynamically focus and steer US energy by manipulating the phase at each element. Linear phased arrays (Nx1 elements) are used in ultrasound imaging to sweep the beam over a cross-sectional plane, and several have been demonstrated for power delivery to US implants [9]–[11]. In this work a planar array (NxM elements) was fabricated to allow for steering to locations within a 3D volume of tissue.

In its simplest implementation, transmit beamforming can be achieved by calculating a time delay for each array element based on the differences of the distances from each element to the implant and the propagation speed in the medium [9]. This requires prior knowledge of the target implant position relative to the array. To localize the implant, a subset of array elements can record either a pulse sent by the implant [12], or a backscattered signal received from the implant [11]. Time delays can be calculated by finding the maximum of the cross-correlation between signals received on the individual array elements. The location of the implant can then be found by solving a nonlinear optimization problem [11]. Once the location is determined, the time delay beamforming method can be applied. This does not account for tissue inhomogeneity and scattering which may distort and redirect the
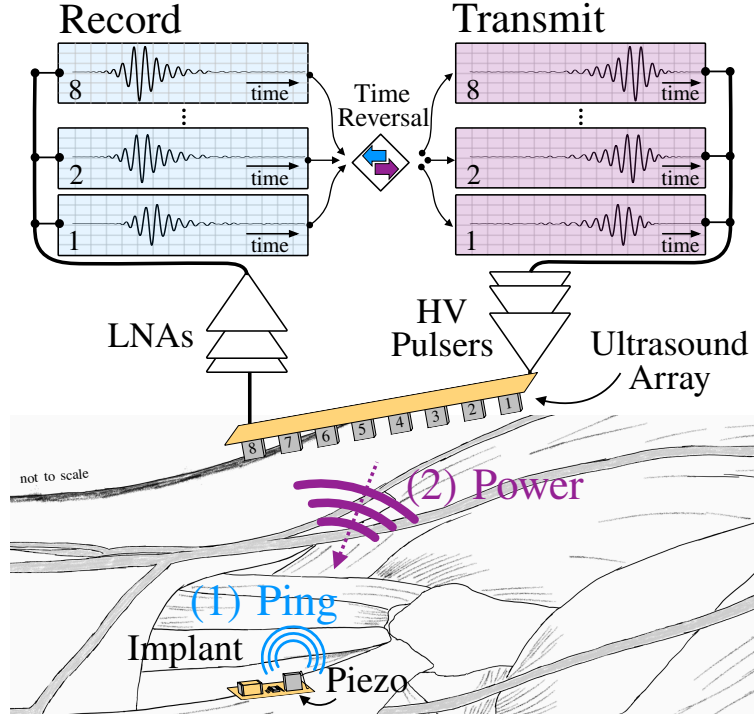
Figure 1.2: Neural implant and cross-section of ultrasound array demonstrating the concept of active uplink time reversal.

beam. In contrast, this work proposes the use of a computationally simple method for ultrasonic beamforming to neural implants that is inherently robust to tissue inhomogeneity and scattering.

1.3   Time reversal

Time reversal (TR) beamforming requires no prior knowledge of the implant position or characteristics of the medium. In a lossless medium, time reversal US beamforming has been shown to be the optimal solution for maximizing pressure at a target [13]. In such a medium, the position and time-varying pressure field $P(\vec{r}, t)$ is described by:

$$\vec{\nabla} \cdot \left(\frac{\vec{\nabla} P}{\rho} \right) - \frac{1}{\rho c^2} \frac{\partial^2 P}{\partial t^2} = 0. \tag{1}$$

The space-varying propagation speed and density are given by $c(\vec{r})$ and $\rho(\vec{r})$, respectively. Since there is only a second-order time derivative, if $P(\vec{r}, t)$ is a solution then $P(\vec{r}, -t)$ must also be a solution. With an additional attenuation term this property is lost, but since attenuation is low in biological tissue this remains a valid approximation [13]. Even in cases

with significant attenuation, such as focusing through the skull, a modified time reversal procedure can be used [14].

An illustration of the "active uplink" time reversal process is shown in Fig. 1.2. The implant sends out an acoustic pulse or "ping" received by the ultrasound array. These signals are recorded from the array elements, reversed in time, and played back to focus acoustic power on the targeted implant. This procedure could be repeated intermittently to correct for the implant shifting relative to the array. To initially power up the implant before the ping, the external ultrasound array would start in a high-power mode and/or sweep its focus using standard time delay beamforming. After the time reversal procedure, the external transducer power would be lowered since power could now be efficiently delivered to the implant.

This procedure assumes the implant can actively drive the piezo; however, many low-power ultrasonic implants communicate with the external transceiver only through passive backscattering [2], [3], [6]. Time reversal can still be implemented in this scenario through a different, iterative pulse-echo procedure. In the iterative method, the transducer array first sends out an unfocused pulse. The implant provides a highly reflective target compared to its surroundings, and the backscatter, or echo, originating from the implant will be received by the array. This echo is reversed in time and played back. Iterating over these steps will result in the US beam converging on the strongest, or brightest reflector [14].

Finally, there is a distinction between true time reversal and using a signal from the implant to calculate the required time/phase shifts between elements [12], which we also demonstrate and refer to as phase reversal. This approach is a specific case of time reversal in which the received signals are composed of a single constant-amplitude sinusoid, and it allows for continuous beamforming. However, in a heterogenous, highly scattering medium, the received signals may not be sinusoidal [15]. Time reversal will still work in these conditions, but it only provides pulses of finite length. This is well-suited for powering US implants since they are placed in inhomogeneous tissue and typically receive transient pulses of power.

Chapter 2 will provide an analysis of planar phased array design considerations and will describe the fabrication of the array used in this work. Design of the ultrasound beamforming system is described in Chapter 3. In Chapter 4, methods and results from experiments testing active uplink time reversal will be shown. Methods and results for iterative time reversal are given in Chapter 5, and Chapter 6 will summarize and discuss future work.

Chapter 2

Phased array design

2.1 Directivity and grating lobes

In this work, a 2D, planar transducer array was designed and fabricated in order to target an implant within a 3D volume of tissue. While this is essential for ensuring implant functionality regardless of lateral misalignment, a planar array has greatly increased system complexity compared to a 1D, linear array. As will be described in subsequent chapters, the custom ultrasound system built for this work uses MAX14808 high voltage digital pulsers. These are controlled using a parallel interface requiring 2 bits per channel. With the finite number of I/O pins on the FPGA being used to control the system, the number of transducer channels that can be independently driven is limited to 52. This results in an 8x8 element planar array with the three elements in each corner removed, as shown in Fig. 2.6.

While the channel number is limited, the pitch (inter-element spacing) and total array aperture may be varied. The choice of pitch of a phased array is a tradeoff between the directivity and the production of grating lobes. The directive gain at a given point is defined as the power density at that point divided by the isotropic power density [16]. The maximum directive gain, commonly referred to simply as directivity, is therefore given by:

$$D = \frac{P_{max}}{P_{average}}$$

For a large array with equal element excitation, the radiation pattern/directivity is the product of the array factor (the directivity resulting from the array geometry) and the directivity of the radiation from each element [17]. In the principal planes, the beam pattern for a planar array is the same as that of a linear array, so a linear array will be considered here for simplicity. The magnitude of the array factor for a linear array with equally spaced elements as a function of angle theta (where 0° is perpendicular to the array) is given by:

$$AF = \frac{sin[N\frac{\pi d}{\lambda}(sin\theta - sin\theta_s)]}{sin[\frac{\pi d}{\lambda}(sin\theta - sin\theta_s)]}$$
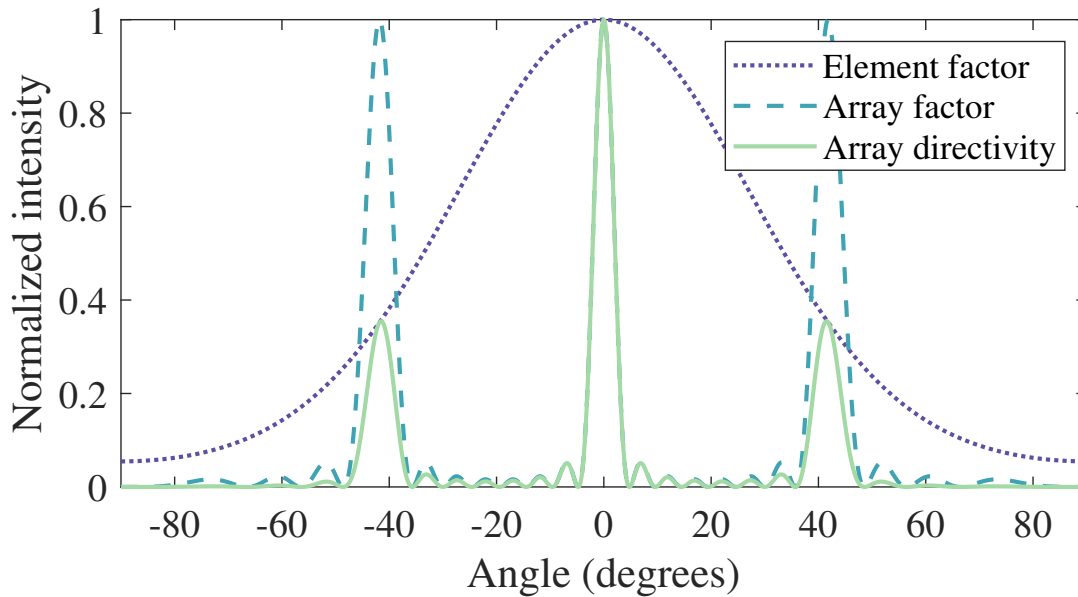
Figure 2.1: Array factor, element factor, and directivity for an 8-element linear array with λ=1 mm, d=1.5 mm.

where θ_s is the desired steering angle, N is the number of elements, and d is the pitch [16], [17]. This function has maxima for $\theta = \theta_s$, and the array factor value at this angle equals N. Thus, the maximum value of the array factor is dependent only on the number of elements. This also holds true for the array factor of planar array, which is approximated by the product of two linear array factors [16].

The array factor will be at a maximum when:

$$\theta = sin^{-1}(\frac{m\lambda}{d} + sin\theta_s)$$

where m is an integer. Depending on the steering angle and ratio of pitch to wavelength, there may be multiple solutions to this equation. This reveals the presence of grating lobes, which can be considered as aliasing resulting from insufficient spatial sampling. Grating lobes are typically avoided in ultrasound imaging because it is impossible to tell whether a signal received by the array originated from the main lobe or a grating lobe. To prevent grating lobes, a pitch is chosen to satisfy:

$$d \leq \frac{\lambda}{1 + sin\theta_{s,max}}$$

To eliminate grating lobes at all steering angles, $d < \lambda/2$ should be chosen (a result of the Nyquist theorem), but a pitch of up to λ can be used without the production of grating lobes
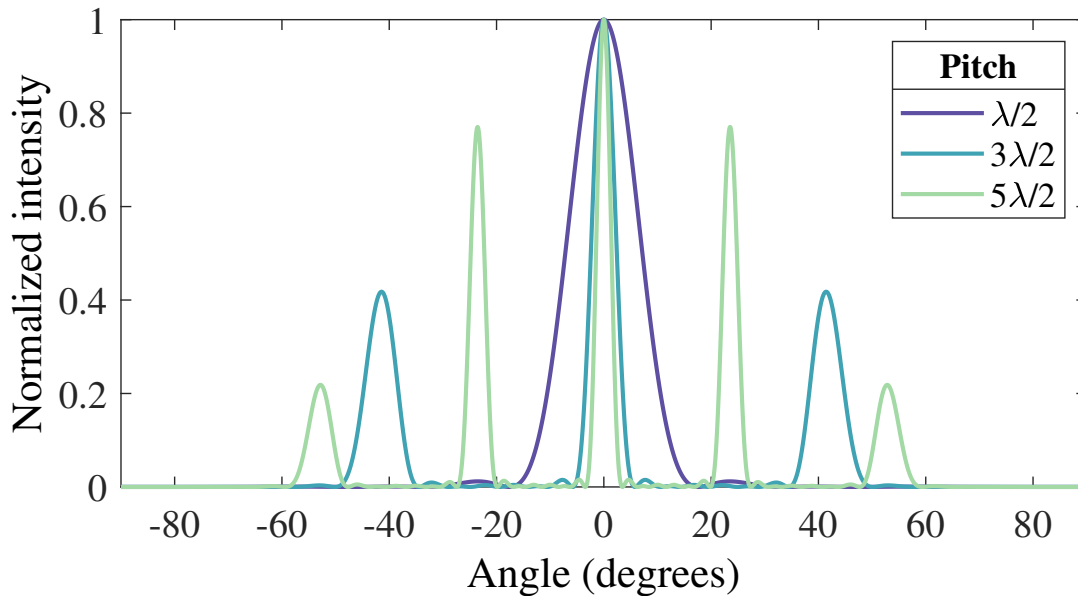
Figure 2.2: Directivity for a 52-element planar array with varying pitch.

if steering to 0°. An example pattern is shown in Fig. 2.1 for a linear array of 8 elements with a d=1.5 mm and λ=1 mm, with a steering angle of 0°. Note the presence of grating lobes, but these are reduced compared to the main lobe due to the element factor.

The beamwidth of a phased array is determined by the total aperture of the array. For a square planar array, the angular beamwidth is $\frac{0.866\lambda}{D}$, where D is the length of a side of the array [16]. Increasing the array aperture narrows the beamwidth. In Fig. 2.2, acoustic intensity as a function of angle is shown for a 52-element planar array, calculated using the MATLAB Phased Array System Toolbox. Note that while increasing the pitch does result in grating lobes and decreased main beamwidth, the maximum power, or array gain, is identical for each configuration. Therefore, as long as the beamwidth is sufficiently larger than the implant piezo and the beam can be accurately steered toward the implant, the grating lobes produced by a larger pitch array are not necessarily detrimental for efficient power delivery to an implant. If multiple implants are used, grating lobes could accidentally power up and receive modulated backscatter from an incorrect implant. However, if maximizing power delivery is the main goal, as is the case for neural stimulation implants, then a large pitch array with grating lobes could be an acceptable approach. This will be further demonstrated in the next section.

2.2   Optimizing pitch for maximum power delivery

The previous analyses have considered the far-field radiation pattern of phased arrays; however, it is also possible for the implant to be operated in the near-field of the array. The near-field, or Fresnel region, of a transducer is where:

$$z < \frac{D^2}{4\lambda}$$

where z is the axial distance to the transducer and D is the transducer diameter [18]. In the near-field region, focusing can be achieved using a phased array in addition to the steering which has already been described for the far-field region [19]. The following analysis will demonstrate why a larger pitch array with grating lobes may be preferable for maximizing total power delivered to an ultrasonic implant. Field II is used for the following simulations [20], [21].

The US FDA limits the spatial peak-temporal average intensity, I_{spta}, of diagnostic ultrasound in the body to 7200 W/m^2 [22]. If the implant is located in the far-field of the array, then the focal point will occur at a shallower depth than the implant. If the implant is located in the near-field of the array, then the acoustic power can be focused at the depth of the implant. The near-field region of a 52-element, 1.5 MHz, planar transducer with $d = \lambda/2$ measures only 3 mm, much shallower than the implant depth.

The near-field region can be extended by increasing the pitch while maintaining a constant number of elements. Acoustic intensity while targeting an implant at 50 mm depth using a 52-element planar array is shown in Fig. 2.3, with a pitch of $\lambda/2 = 0.5$ mm in (a) and a pitch of $2\lambda = 2.0$ mm in (b). Both arrays are targeting an implant located at 50 mm depth (Z axis), which is shown roughly to scale as a black square. The array drive voltage has been scaled such that the I_{spta} is equal in both cases. In addition to producing grating lobes, increasing the pitch relative to wavelength leads to a pattern of high intensity regions near the transducer, shown observed in Fig. 2.3(b). Unless an acoustic spacer is used, these high intensity regions will be present within the tissue and must be considered when attempting to maximize power delivered to the implant.

Fig. 2.4 shows the axial time-averaged acoustic intensity for 52-element planar arrays of increasing pitch focused at a depth of 5 cm. A constant element drive voltage is used for each pitch configuration in Fig. 2.4(a). While the intensity at 5 cm is nearly constant across all pitch configurations, the peak intensity is lower with a larger pitch. Therefore, for the larger arrays, the drive voltage can be increased to increase the maximum power delivered to the implant. Fig. 2.4(b) shows the results of this rescaling which sets the I_{spta} for each configuration equal to the FDA limit of 7200 W/m^2. The array with a 4 mm pitch results in over an order of magnitude improvement in acoustic intensity at the target compared to the array with a 0.5 mm pitch, but this comes at the cost of producing 48 grating lobes when focused at $0°$.
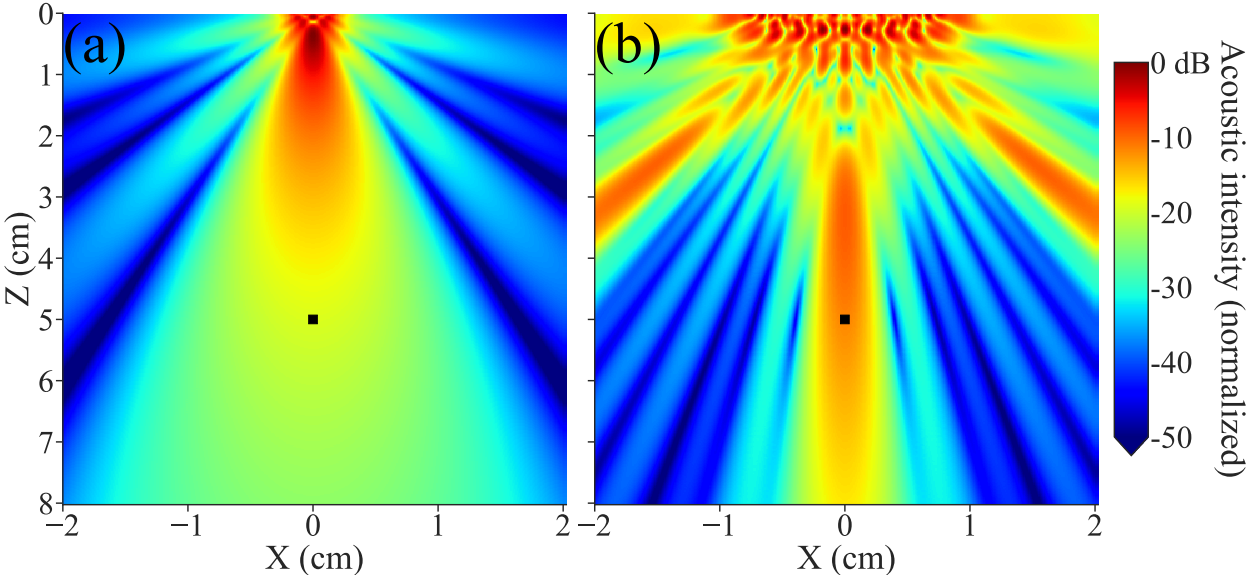
Figure 2.3: Simulated acoustic intensity (in dB) for a 52-element planar array with a pitch of (a) 0.5 mm and (b) 2.0 mm with $\lambda = 1.0$ mm when targeting an implant (black square) located at 50 mm depth. Results for each have been scaled to have an equal I_{spta}.
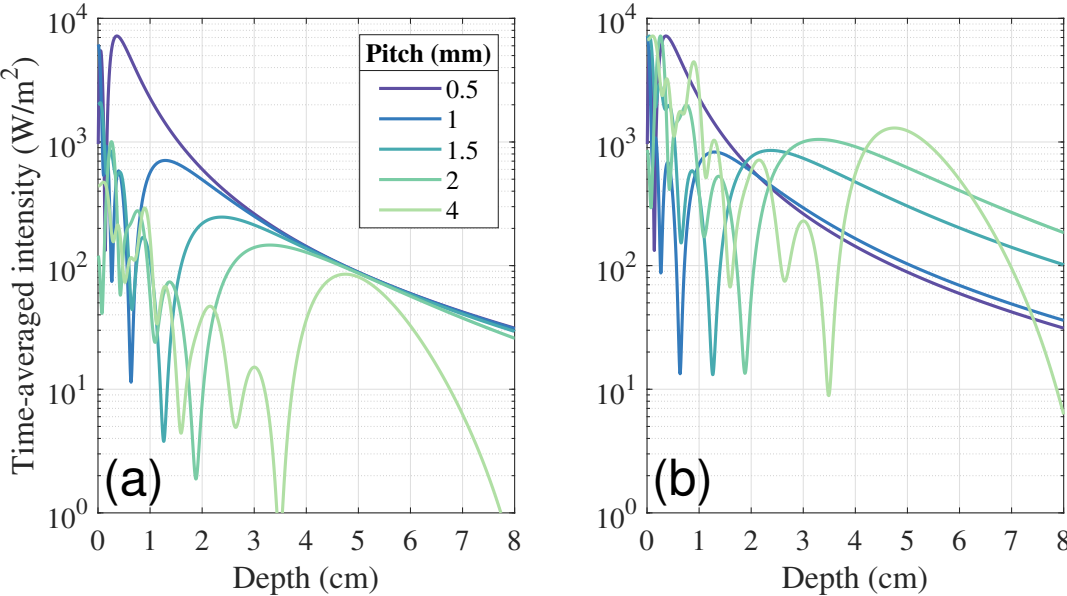
Figure 2.4: Simulation of time-averaged intensity along axis while varying pitch for a 52-element planar array focused at 5 cm depth. In (a) a constant drive voltage is used for all configurations, while in (b) the drive voltage is scaled for each configuration such that I_{spta}=7200 W/m^2.
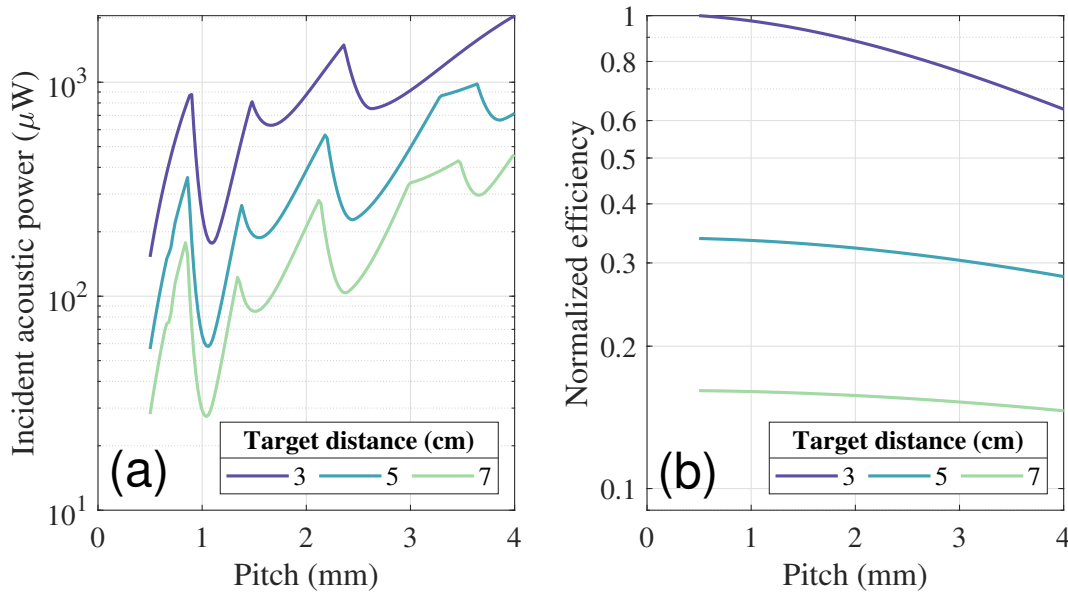
Figure 2.5: (a) Simulated maximum allowable incident acoustic power on piezo target while meeting FDA I_{spta} limit. (b) Simulated power transfer efficiency (normalized) from transducer to piezo.

The rescaling of drive voltage for larger pitch arrays results in a greater total acoustic power entering the tissue but allows for more power to be delivered to an implant without exceeding the FDA I_{spta} limit when compared to a smaller array. Using this rescaling approach to set I_{spta} to the FDA limit and sweeping values for pitch, Fig. 2.5(a) shows the incident acoustic power on the face of a 0.8 mm cube piezo. This is calculated by integrating the simulated intensity over the piezo face and thus takes into account the decreased beamwidth with increasing pitch. The normalized power transfer efficiency from the transducer array to the piezo is shown in Fig. 2.5(b). This efficiency is constant regardless of the scaling factor and does not decrease significantly with increasing pitch.

The maxima and minima in Fig. 2.5(a) result from the intensity pattern in the near-field, which is dependent on the exact acoustic properties of the tissue and is difficult to predict. These results should not be used to determine an optimal pitch since this will change depending on implant depth and tissue properties. Rather, they lead to the general conclusion that, with a limited number of channels available, a pitch larger than $\lambda/2$ may be chosen if the goal is to maximize power safely delivered to an implant. However, if the goals are to improve the overall system efficiency, reduce the total acoustic power dissipated in the tissue, or eliminate grating lobes, then a smaller pitch should be used.
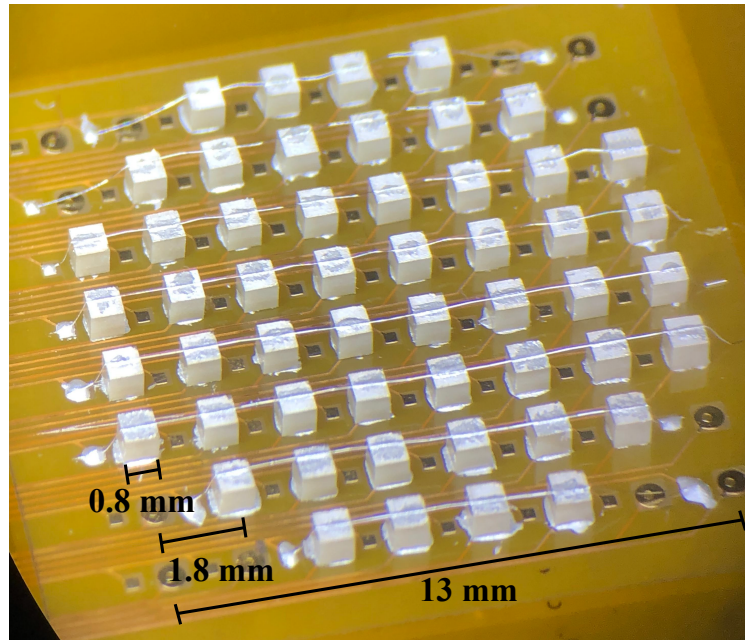
Figure 2.6: Fabricated 52-element planar array used in this work.

2.3   Array fabrication

After consideration of the preceding design tradeoffs for an ultrasound phased array used to power an implant, a pitch of 1.8 mm was chosen for the planar array. While using a limited number of elements, this results in a good compromise between maximizing overall efficiency, maximizing intensity at the implant while meeting FDA limits, and minimizing the number of grating lobes produced. A total of eight grating lobes are expected to be produced, with four at 33° and four at 51° from the axis when focused at 0° [16].

The 52-element, 13 mm diameter planar array was assembled on a 0.3 mm polyimide flexible printed circuit board. Lead zirconate titanate piezoceramic (APC851) was diced into 0.8 mm cubes, and these elements were attached with silver epoxy (EPO-TEK H20E). The top ground electrodes were connected using bonding wire and silver epoxy. An image of the array is shown in Fig. 2.6. Piezo dicing was performed by Nathan Ersumo, and the array assembly was completed by Mohammad Meraj Ghanbari. Additional backing and matching layers can be added to improve efficiency and protect the elements [8]. Impedance measurements revealed only 4 defective elements; the remainder showed good matching with each other and with finite element model simulations [7]. The series and parallel resonant frequencies of these array piezos were measured to be 1.5 and 1.75 MHz, respectively.

Chapter 3

Ultrasound system design

3.1 First generation system

The custom ultrasound beamforming system incorporates the MAX14808, an octal three-level high-voltage digital pulser with integrated T/R switch which has been used in various studies with ultrasonic implants [10], [23]. Each ultrasound channel is controlled by two logic inputs, and the devices are run in a transparent (as opposed to clocked) mode, meaning that the pulser outputs directly reflect the input logic after a short delay. A beamforming system requires a high number of channels, and so there are a large number of control signals on this parallel interface. A Spartan-6 LX150 FPGA within an Opal Kelly XEM6010 is used to generate the control signals, control the receive signal multiplexers, receive data from the parallel ADC interface, and communicate with a PC over USB. The finite number of I/O pins on this device limits the number of pulser channels to 52.

The first generation of the system, shown in Figs. 3.1(a) and 3.2(a) was designed by Mohammad Meraj Ghanbari and used in previous publications [1], [24]. It uses eight MAX14808 evaluation boards which are attached via header connectors to a base PCB (the "Main Board"). This arrangement and the parallel control interface is a non-optimal solution, but the intention was to reduce development time of the system by minimizing firmware complexity while using fully tested ultrasound pulser boards. A ribbon cable connects the pulser outputs to the "Mini" board which attaches to the flex-PCB piezo array and also contains op-amps which serve to buffer and provide amplification to received ultrasound signals when in receive mode. This is intended to prevent attenuation of the signal due to the cable and other parasitic capacitance. These buffered signals are delivered to the Main board for analog-to-digital conversion via a second ribbon cable. Only one ribbon cable is connected at a time, and this configuration must be changed between transmit and receive modes. This system was used to collect the data for active uplink time reversal in Chapter 4.
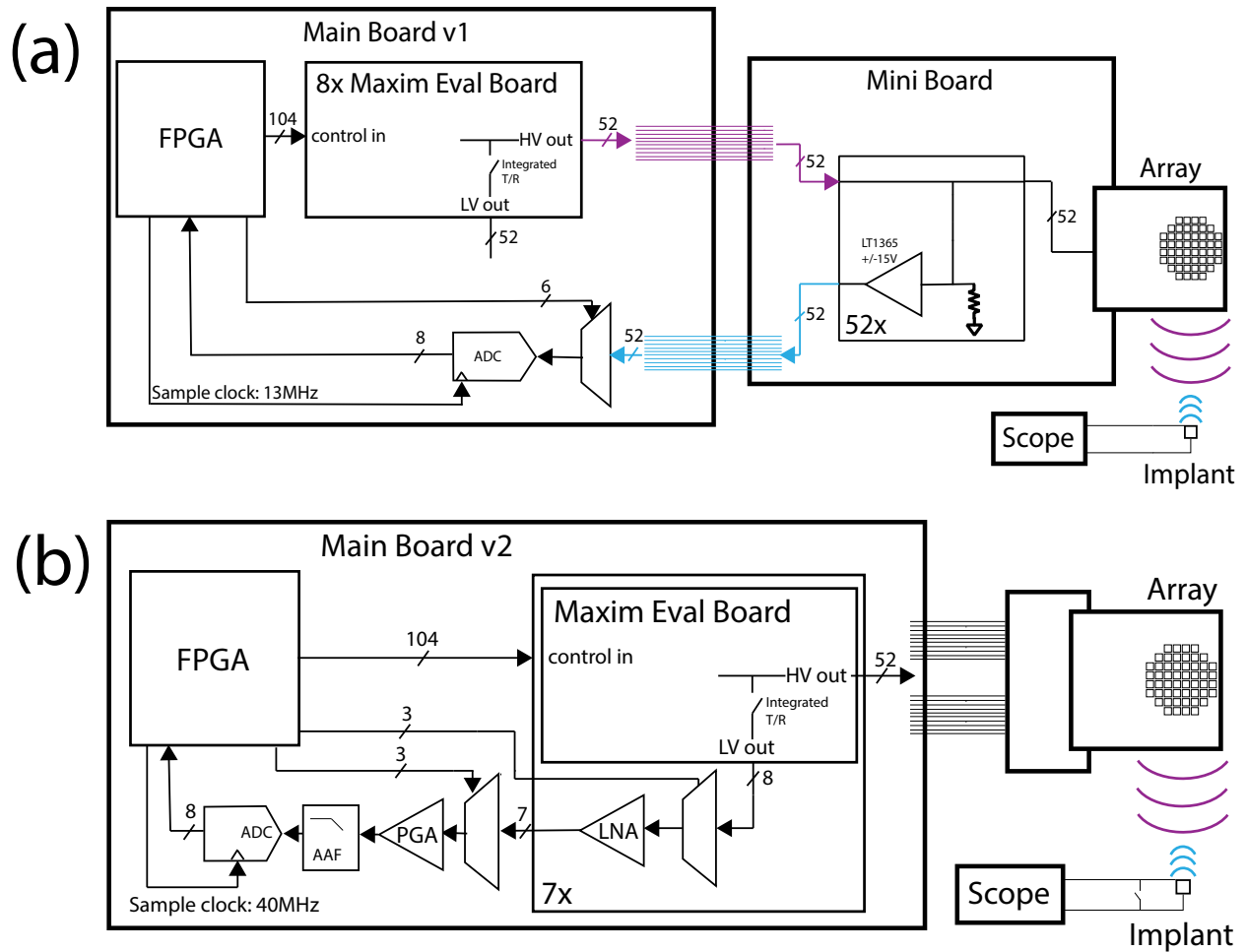
Figure 3.1: (a) 1st generation ultrasound system (b) 2nd generation ultrasound system

3.2   Second generation system

The 1st generation system suffers from a number of design issues primarily related to signal integrity which limited its performance and prevented it from functioning in pulse-echo mode (which requires simultaneous transmit and receive functionality). Below, these issues and how they are addressed in Main Board Gen 2 are described. The 2nd generation system is shown in Fig. 3.1(b) and the Main Board Gen 2 layout is Fig. 3.2(b). This was used to collect the data for iterative time reversal in Chapter 5.

Ground plane

The first generation 2-layer PCB design does not have a ground plane. While this reduces trace capacitance, the lack of a low-impedance current return path for high frequency signals
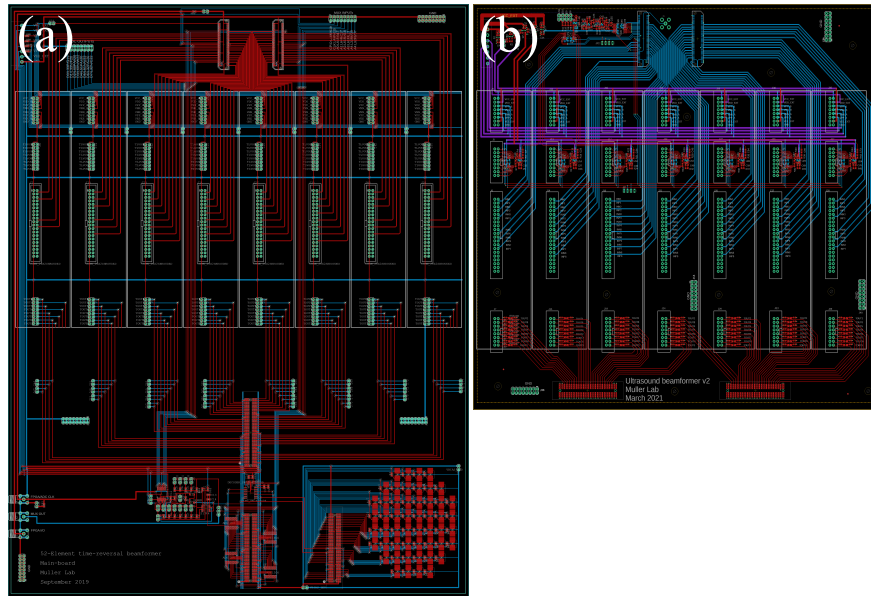
Figure 3.2: (a) Main Board Gen 1 and (b) Main Board Gen 2 layouts shown to relative scale.

causes many issues and is generally a poor design choice. The new 4-layer board includes a ground plane. While it can be beneficial to separate the board into regions with analog vs digital ground, the requirements of this board to interface with the MAX14808 evaluation boards (which have a single ground) made this impractical and likely to result in additional issues. Therefore, a single unbroken ground plane is used, with digital and analog signals separated and crossing at 90 degree angles.

ADC placement

On Main Board Gen 1, the ADC is placed on the opposite side of the board from the FPGA, requiring long clock and data traces between the two. While the ADC is rated for 80 MSPS, the long trace length limits maximum sampling rate to 13 MSPS. Additionally, the long single-ended ADC clock trace without a ground plane results in interference on the signals being measured. This necessitates averaging of the received signals over multiple measurements, which increases data acquisition time. In the new design, the ADC is located close to the FPGA, reducing interference and allowing the ADC to sample at 40 MSPS without the need for averaging.

Crosstalk between channels

To reduce crosstalk between channels, commercial ultrasound systems use individually shielded micro-coax cables to connect the system to the probe [25]. However, ribbon cables

are less expensive and more convenient to assemble than individual cables. The first generation design uses an 80 conductor cable, and most of the 52 signals are directly adjacent to other signals. This results in clearly visible crosstalk between channels. To reduce this issue, the ground-signal-ground (G-S-G) connection pattern is used so that all signals have a return path and no signals are adjacent to one another [26]. Two 68 conductor ribbon cables used in the 2nd generation.

T/R switch

The first generation system has 52 unity-gain buffers (LT1365) located on the "Mini Board" near the array. The non-inverting input of these buffers is connected directly to the output from the high voltage pulsers. Since the op-amps have a maximum supply voltage of ±15 V, this reduces the allowable output from the high voltage pulsers from ±105 V to ±15 V to satisfy the absolute maximum input ratings, degrading the maximum possible SNR. However, in practice driving the pulsers with ±15 V is not possible because this greatly increases the op-amp power consumption and causes stability issues. Therefore, a ±5 V supply is used for the "high voltage" pulsers in the 1st generation system, resulting in ±3.3 V driving the piezos after two on-chip diode drops.

In commercial ultrasound systems, isolation between the high-voltage transmit circuits and low-voltage receive electronics is accomplished using transmit/receive (T/R) switches [19]. The MAX14808 chips include integrated T/R switches and low-voltage receive outputs which are used in the 2nd generation design to allow it to function in pulse-echo mode. This does result in signal attenuation from the approximately 150 pF parasitic capacitance due to the ribbon cables, routing, and switches. Isolating the amplifiers from the drivers allows the high voltage pulsers to be supplied up to ±25 V, the limit of the power supplies used.

Power consumption

To limit system complexity and data rate requirements, a single ADC is used in both generations. However, the 1st generation uses a buffer for each channel and requires ~400 mA total quiescent current for the buffers alone. This causes significant heating of the Mini Board, making it impractical to incorporate into an actual probe head. In the new design, the 8 low voltage receive signals per channel are multiplexed (MAX4638) on the Main Board before amplification. While this adds 54 pF parasitic capacitance per channel, this is just part of the estimated 150 pF total parasitic capacitance per channel. Only 7 low voltage amplifiers are then required after the muxes, greatly reducing the total system power consumption.

Separate analog power supplies

Main Board Gen 1 uses the same supplies for the digital HV pulsers, amplifiers, and ADC. The revised design generates the analog supplies used for the amplifiers and ADC from

low-noise, high-PSRR LDOs (TPS7A20 and TPS723).

Anti-aliasing filter

The 1st generation does not include an anti-aliasing filter before the ADC, which should be used to prevent high-frequency noise from folding into the signal bandwidth when sampling. The new design includes a 4th-order Bessel filter with $f_c = 5$ MHz constructed from two op-amps (OPA355) in a multiple feedback topology. The Bessel filter was chosen due to its maximally flat group delay to accurately record any harmonics in the time domain. A 2nd-order filter would likely be sufficient for this application, but using an additional op-amp also provides the opportunity to add gain.

Supply decoupling

The 1st generation design includes decoupling capacitors between the supply rails rather than between the supply rails and ground, which was problematic since the signals were referenced to ground. The 2nd generation uses decoupling capacitors between each supply and ground placed closer to the power pins.

Option for matching network

Impedance matching networks can be used to match the impedance of the pulser outputs with the impedance seen looking toward the ultrasound transducers, increasing the power delivered to the load [27]. The Main Board Gen 2 includes pads to add a pi configuration matching network, although this was not used in this work.

Board area

The Main Board Gen 1 uses eight MAX14808 evaluation boards and measured 43x34 cm. The Main Board Gen 2 uses only seven MAX14808 boards (with the same number of usable channels) and measures 30x27 cm. This area reduction can be seen in Fig. 3.2.

3.3 Low-noise amplifier configuration and selection

In the 2nd generation system, the backscattered acoustic signals are received on the array and connected to the low voltage outputs of the MAX14808 using integrated T/R switches. The signals are then multiplexed to reduce the channel count by 8x, then amplified by a low-noise amplifier (LNA). These amplified signals are routed to another multiplexer, then to a programmable gain amplifier, then to the anti-aliasing filter, then to the ADC. Due to the small magnitude of the received backscatter signals, minimizing noise is important to the system design. Since the first amplifier provides substantial gain, the signal to noise ratio

(SNR) is set by the noise at this stage. To compare between amplifier configurations and gains, this noise should be referred back to the input, the piezo voltage source.

While the frequency dependent response of piezo can be represented by equivalent circuit models such as the Redwood model, at resonance it can be reduced to a Thevenin equivalent circuit [7]. Frequency components outside a band surrounding the resonance frequency range will be removed by analog and digital filtering, so noise at the resonant frequency will be the most important to reduce. Therefore, the Thevenin model is used for analytical calculations of input-referred spot noise at the piezo resonant frequency. This piezo source resistance, R_s, is estimated to be 2.2 kΩ based on measurements and finite model simulations for a 0.8 mm cube piezo [7].

In parallel with the piezo is a parasitic capacitance C_p, which consists of capacitance of PCB routing, ribbon cables (17.3 pF/foot * 2 feet), interconnects, capacitance on the MAX14808 ultrasound pulsers, and the switch on capacitance of the MAX4638 multiplexer (54 pF). In total, the parasitic capacitance is estimated to be 150 pF. At the 1.5 MHz piezo resonant frequency, the magnitude of this parasitic impedance is 700 Ω, resulting in a 75% reduction in signal amplitude. While this equally reduces noise from the source resistance, it does not reduce all amplifier noise components and consequently reduces SNR.

In selecting an op-amp to use for the LNA, there is a fundamental tradeoff between those using BJT and CMOS devices. BJT devices (high current noise and low voltage noise) are typically appropriate when there is a low-impedance source, and CMOS (low current noise and high voltage noise) is used for a high-impedance source. Ranging from around 2kΩ to 20kΩ depending on the resonance used, the array piezos present an intermediate impedance. Therefore, analysis and SPICE simulation was performed to determine the optimum device choice and amplifier configuration for this system. The OPA355 (CMOS) and OPA846 (BJT) were chosen for comparison due to their low noise, sufficient gain-bandwidth product, and convenient supply voltage range. Important parameters are given in Table 3.1. Inverting, non-inverting, and transimpedance amplifier configurations were analyzed. In the following calculations, v_n is the op amp noise voltage and i_{nn},i_{np} are the op amp current noise at the negative and positive inputs. These are specified at 1 MHz and are assumed to be independent for these calculations.

Table 3.1: Relevant parameters for the OPA355 and OPA846 [28], [29].

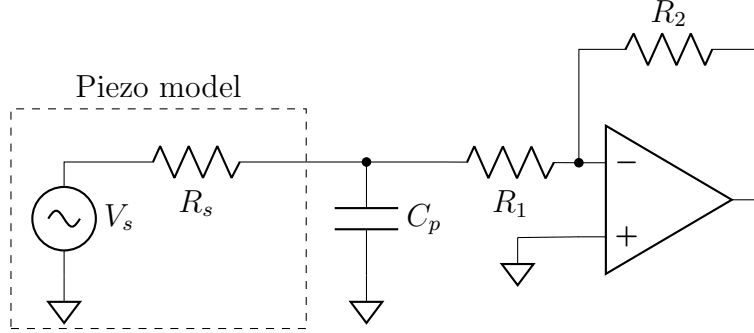|	OPA355	OPA846
Device type	CMOS	BJT
Gain-bandwidth (MHz)	200	1750
Voltage noise (nV/rHz)	5.8	1.2
Current noise (pA/rHz)	0.05	2.8
Input bias current (nA)	0.003	1900

Inverting amplifier

Figure 3.3: Inverting amplifier with piezo model and parasitic capacitance.

The inverting amplifier provides flexibility to be used in other configurations such as a transimpedance amplifier. Note that for an op amp with a significant input bias current, such as the OPA846, a resistor must be placed on the noninverting input to cancel the offset from the input bias current. The thermal noise from this resistor and the resulting current noise at this input can be effectively eliminated with a large parallel capacitor, and so it is ignored in this analysis.

$$\overline{v_{no,R_s}^2(f)} = 4k_BTR_s \left| \frac{R_2}{R_1 + R_s + sC_pR_1R_s} \right|^2$$

$$\overline{v_{no,R_1}^2(f)} = 4k_BTR_1 \left| \frac{R_2(1 + sC_pR_s)}{R_s + R_1(1 + sC_pR_s)} \right|^2$$

$$\overline{v_{no,R_2}^2(f)} = 4k_BTR_2$$

$$\overline{v_{no,v_n}^2(f)} = v_n^2 \left| \frac{(R_1 + R_2)(1 + sC_pR_s) + R_s}{R_1(1 + sC_pR_s) + R_s} \right|^2$$

$$\overline{v_{no,i_{nn}}^2(f)} = i_{nn}^2 R_2^2$$

$$\overline{v_{no,i_{np}}^2(f)} = 0$$

$$\overline{v_{no,sum}^2(f)} = \overline{v_{no,R_s}^2(f)} + \overline{v_{no,R_1}^2(f)} + \overline{v_{no,R_2}^2(f)} + \overline{v_{no,v_n}^2(f)} + \overline{v_{no,i_{nn}}^2(f)} + \overline{v_{no,i_{np}}^2(f)}$$

$$\overline{v_{n,in}^2(f)} = \frac{\overline{v_{no,sum}^2(f)}}{\left| \frac{R_2}{R_1+R_s+sC_pR_1R_s} \right|^2}$$
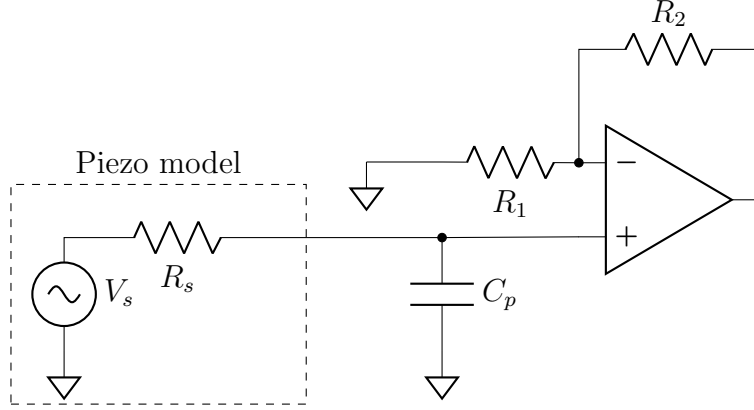
Non-inverting amplifier

Figure 3.4: Non-inverting amplifier with piezo model and parasitic capacitance.

The non-inverting amplifier has the advantage of high input impedance, which is useful when amplifying a voltage signal with high source impedance. However, due to the parasitic capacitance which already acts as a voltage divider, the high input impedance of the amplifier itself is less significant.

$$\overline{v_{no,R_s}^2}(f) = 4k_B T R_s \left| \frac{R_1 + R_2}{R_1(1 + sC_P R_s)} \right|^2$$

$$\overline{v_{no,R_1}^2}(f) = 4k_B T R_1 \left| \frac{R_2}{R_1} \right|^2$$

$$\overline{v_{no,R_2}^2}(f) = 4k_B T R_2$$

$$\overline{v_{no,v_n}^2}(f) = v_n^2 \left| \frac{R_1 + R_2}{R_1} \right|^2$$

$$\overline{v_{no,i_{nn}}^2}(f) = i_{nn}^2 R_2^2$$

$$\overline{v_{no,i_{np}}^2}(f) = i_{np}^2 \left| \frac{R_s(R_1 + R_2)}{R_1(1 + sC_p R_s)} \right|^2$$

$$\overline{v_{no,sum}^2}(f) = \overline{v_{no,R_s}^2}(f) + \overline{v_{no,R_1}^2}(f) + \overline{v_{no,R_2}^2}(f) + \overline{v_{no,v_n}^2}(f) + \overline{v_{no,i_{nn}}^2}(f) + \overline{v_{no,i_{np}}^2}(f)$$

$$\overline{v_{n,in}^2}(f) = \frac{\overline{v_{no,sum}^2}(f)}{\left| \frac{R_1 + R_2}{R_1(1 + sC_P R_s)} \right|^2}$$

Transimpedance amplifier
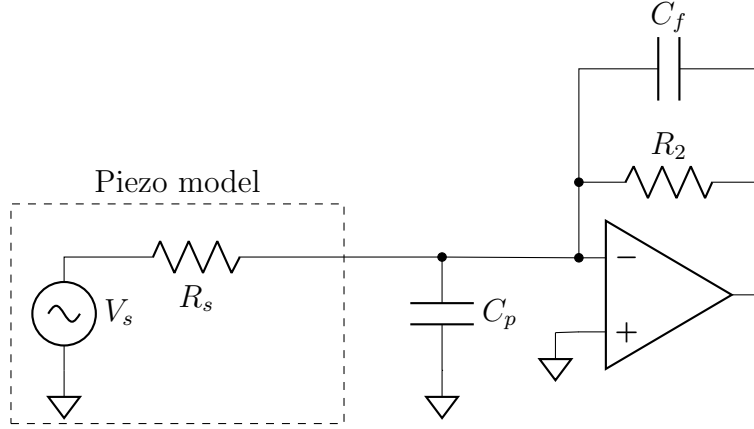
Figure 3.5: Transimpedance amplifier with piezo model and parasitic capacitance.

The transimpedance amplifier (TIA) is an attractive topology for this application because the parasitic capacitance C_p does not result in signal attenuation. However, the gain will depend on the internal resistance of the piezo, R_s.

$$\overline{v_{no,R_s}^2(f)} = 4k_BTR_s \left| \frac{R_2}{R_s(1 + sC_fR_2)} \right|^2$$

$$\overline{v_{no,R_2}^2(f)} = 4k_BTR_2 \left| \frac{1}{1 + sC_fR_2} \right|^2$$

$$\overline{v_{no,v_n}^2(f)} = v_n^2 \left| 1 + \frac{R_2(1 + sC_pR_s)}{R_s(1 + sC_fR_2)} \right|^2$$

$$\overline{v_{no,i_{nn}}^2(f)} = i_{nn}^2 \left| \frac{R_2}{1 + sC_fR_2} \right|^2$$

$$\overline{v_{no,i_{np}}^2(f)} = 0$$

$$\overline{v_{no,sum}^2(f)} = \overline{v_{no,R_s}^2(f)} + \overline{v_{no,R_2}^2(f)} + \overline{v_{no,v_n}^2(f)} + \overline{v_{no,i_{nn}}^2(f)} + \overline{v_{no,i_{np}}^2(f)}$$

$$\overline{v_{n,in}^2(f)} = \frac{\overline{v_{no,sum}^2(f)}}{\left| \frac{R_2}{R_s(1+sC_fR_2)} \right|^2}$$

Comparison

The results of calculations comparing the input-referred spot noise at 1.5 MHz for amplifier configurations and op-amps is shown in Fig. 3.6, as a function of R_1. Integrated input-referred noise calculated using SPICE and using the full Redwood model of the piezos rather than the Thevenin equivalent is provided in Table 3.2. Both analyses show that the OPA846 TIA results in the lowest input-referred noise. A comparison of the calculated noise figure of the OPA846 TIA configuration with data from the AFE5804, a commercial fully-integrated analog front-end, is given in Table 3.3. While the commercial front-end does have better performance, the difference is <1 dB.

However, the OPA846 does have significant input bias current due to the BJT devices. Preliminary testing with the OPA846 indicated that this could cause issues when switching between pulser channels even after including a DC current path due to the differing DC resistance of the MAX14808 pulser channels. Also, the TIA configuration had not been used in the 1st generation and it was unknown if any other issues could arise. Therefore, the initial assembly of the 2nd generation board used OPA355 devices in a non-inverting configuration. Since both devices use the same package, the boards can be easily converted to a non-inverting or transimpedance configuration using the OPA846 if noise performance turns out to be a limiting factor for the system.
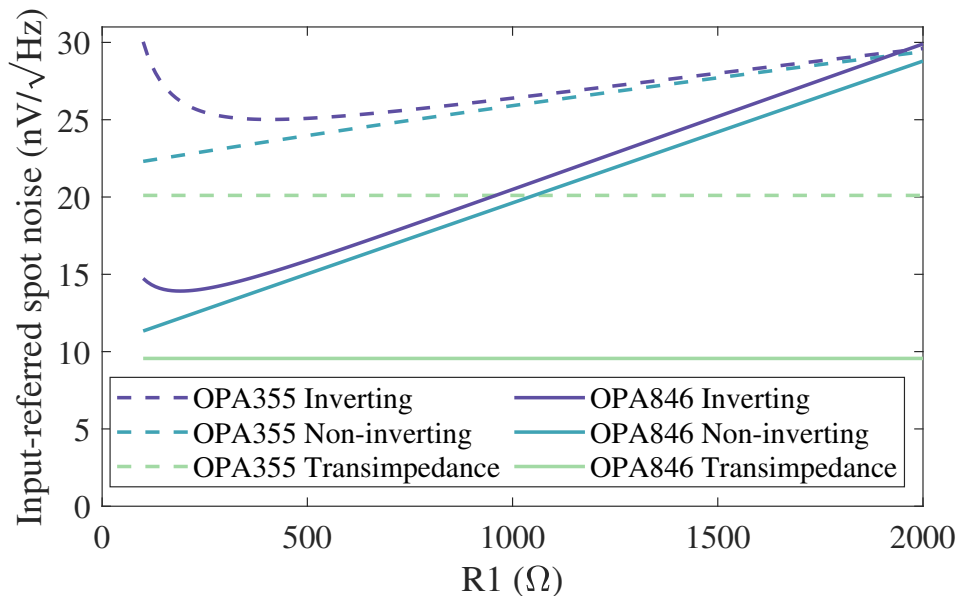
Figure 3.6: Calculation of input-referred spot noise at 1.5 MHz for the OPA355 and OPA846 in inverting, non-inverting, and transimpedance configurations.

Table 3.2: Integrated (1-2 MHz) input-referred noise (μV_{RMS}) using SPICE and the Redwood piezo model for the OPA355 and OPA846 in inverting, non-inverting, and transimpedance configurations.

	OPA355	OPA846
Inverting	1.6	1.26
Non-inverting	1.49	1.17
Transimpedance	1.29	0.58

Table 3.3: Calculated noise figure (dB) for varying source resistance, R_s, and comparison with a commercial fully-integrated ultrasound analog front-end [30]. All data is at 1.5 MHz.

R_s	Commercial front-end (AFE5804)	OPA846 TIA configuration
200	1.1	2.0
400	1.2	1.7
1000	1.8	2.5

Chapter 4

Active uplink time reversal

4.1 Methods
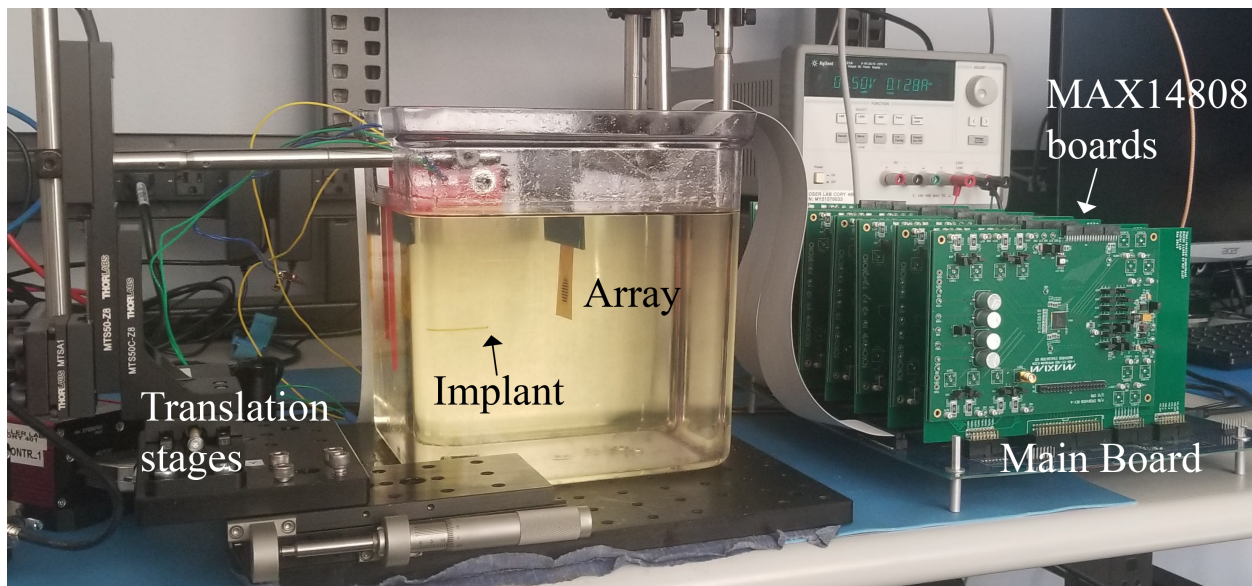
Figure 4.1: Photograph of experimental setup.

The results in this chapter were obtained using the 1st generation ultrasound system. In power/transmit mode (Fig. 3.1, purple), the pulsers drive the array elements at ± 3.3 V from a ± 5 V supply (1.7 V of diode drops), resulting in approximately 1.4 mW consumed by each element. The voltage received by a 0.8 mm cube "implant" piezo is recorded using an oscilloscope and differential probe (Keysight N2750A). Both the array and implant are submerged in canola oil. The perpendicular distance between the array and implant, or implant depth, is controlled by a manual translation stage. The lateral position of the

implant is controlled by a pair of motorized translation stages (Thorlabs MTS50), which allows measurements to be acquired across a plane at a given depth. The experimental setup is shown in Fig. 4.1.

In ping/receive mode (Fig. 3.1, blue), the implant piezo is driven by an US pulser for ten cycles at 1.5 MHz. Op-amps (LT1365) are located close to the array board to buffer and amplify the received signals. These buffered signals are multiplexed to a single 8-bit analog to digital converter (ADC) (ADG9057), and the 40 MHz digitized signals are transferred to a PC. Recording from the entire array thus requires 52 identical pulses to be sent from the implant piezo; in a full implementation, these pulses could be synced based on a command sent from the array to the implant.

After being transferred to the PC, the recorded signals from the "ping" are bandpass filtered and reversed in time. Signals are rescaled by the maximum value for each channel and quantized for the 3-level ($-V_{High}$, 0, $+V_{High}$) US pulsers. This could be implemented with simple digital processing and memory on-chip. As a comparison to time reversal, phase reversal is also used. Here, the implant is driven for only a single cycle, and the phase offsets between the signals received on the array are calculated by finding the maximum of the cross-correlation between the signals. These phase offsets are reversed and used to generate the waveforms for each array element. Finally, time delay beamforming is also used to target the implant using its known position.

The total energy transmitted from the array is estimated from the voltage waveforms applied to the 52 array elements and the element impedance at resonance:

$$E_{transmitted} = \sum_{i=1}^{52} \int_0^T \frac{V_i^2(t)}{R_{Th,array}} dt.$$

Available received energy at the implant is calculated using the recorded voltage waveform and assuming a matched load (2.2 kΩ) for the piezo at series resonance:

$$E_{received} = \int_0^T \frac{V_{implant}^2(t)}{4R_{Th,implant}} dt.$$

Energy transfer efficiency is found by dividing received energy by transmitted energy. Efficiency is used to compare methods because the applied voltage waveforms for time reversal are not explicitly controlled and may slightly differ in duration from other beamforming methods. The results must therefore be normalized for equal input energies.

4.2   Results

Acoustic Field Characterization

Energy transfer efficiency for a cross-section of the acoustic field when focusing at -10° is shown (Fig. 3). This was characterized in the homogeneous oil medium (c ≈ 1470 m/s, $\rho \approx 910$ kg/cm^3, $\alpha \approx 0.15$ dB/cm) at a depth of 5 cm and through 2.5 cm of porcine muscle tissue (c ≈ 1580 m/s, $\rho \approx 1070$ kg/cm^3, $\alpha \approx 2$ dB/cm) suspended in the oil medium at a total depth of 5 cm. Attenuation was greater through tissue, but the half-power beamwidth in both cases was 3.8° (3.3 mm diameter at 5 cm depth), which is consistent with the 3.7° theoretical beamwidth for this array [16].

Time reversal resulted in the highest peak efficiency, while phase reversal resulted in 83% and 77% efficiency when compared to time reversal in oil and tissue, respectively. Phase reversal was similar to time reversal since the porcine tissue was still a fairly homogeneous medium and the US pulsers only had 3-level drive. However, phase reversal required greater computational complexity. Efficiency using calculated time delays was approximately 65% compared to time reversal and required knowledge of the implant position.

Steering to -10° allowed for measurement of a predicted grating lobe resulting from the array pitch. When focusing on a target at 0° at 5 cm depth, the peak-to-peak voltage at the focal point in oil was 0.95 V, which results in 13 μW available power for the implant with only a ±5 V supply for the phased array.
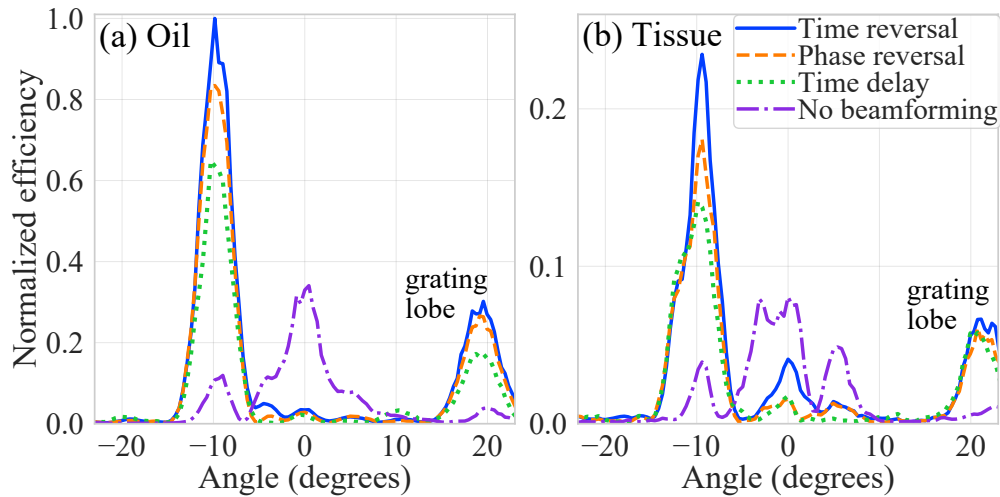

Figure 4.2: Efficiency (normalized to peak time reversal measurement) as a function of angle when focused to -10° through (a) the homogeneous oil medium and (b) 2.5 cm porcine tissue suspended in the oil medium. Note the rescaled y-axis in (b) due to greater attenuation through tissue. Measurements taken at 5 cm depth.
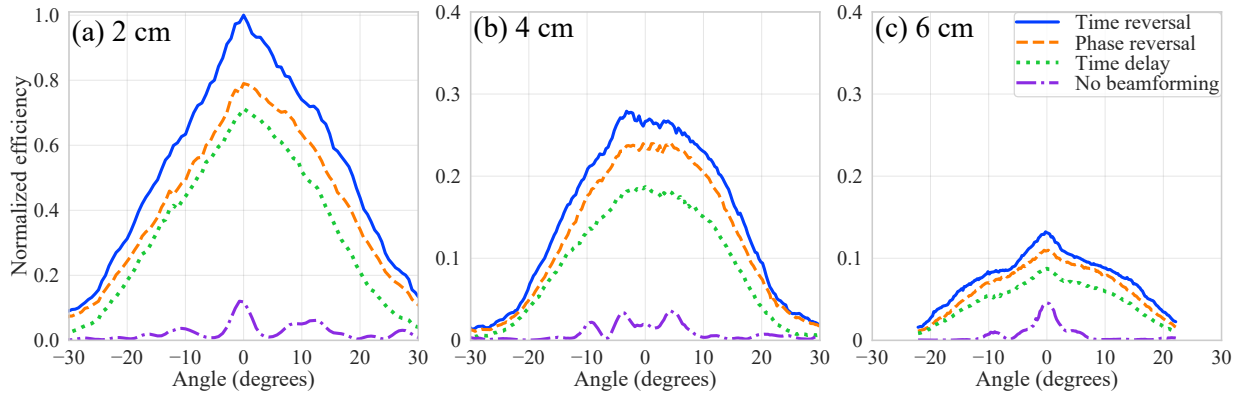
Figure 4.3: Efficiency vs beamforming angle (normalized to peak time reversal measurement at 2 cm) when focusing at each position using time reversal, phase reversal, and time delay beamforming. Measurements were taken at depth planes of (a) 2 cm, (b) 4 cm, and (c) 6 cm. Measured angles were smaller in (c) due to limited translation stage travel. Note the rescaled y-axis in (b) and (c).

Beam Steering and Focusing

The ability to steer and focus on targets at varying angles and depths is shown in Fig. 4.3. Time and phase reversal were performed at each point. As a comparison, results with time delay beamforming using the known implant location and without beamforming are also shown. Efficiency drops off at larger steering angles due to increased beamwidth and increased angular misalignment that results from fixed implant orientation. Time reversal had 10 – 20% greater efficiency than phase reversal across all angles, and both methods performed better than time delay beamforming, especially at larger angles. All methods improved efficiency compared to the unfocused array, with a 2.5x to 100x improvement using time reversal depending on position.

Multiple Implants

An advantage of a phased array system compared to a single-element transducer is the possibility of powering and communicating with multiple implants in different locations. This can occur one at a time using time-division multiplexing or simultaneously using techniques such as code-division multiple access [24], [31]. In the latter case, all implants must receive sufficient power to operate simultaneously. A previously demonstrated approach to powering multiple implants simultaneously was to partition the array and use half to target each implant [10]. In this work, the principle of superposition was used to simultaneously target multiple implants by playing back the sum of the time-reversed signals from each implant.

Two implants at 5 cm depth were powered separately (Fig. 4.4(a),(b)), together using a

partitioned array (Fig. 4.4(c)), and together using superposition (Fig. 4.4(d)). Time reversal was used to generate the transmitted waveforms. Superposition resulted in 0.6x and 0.43x efficiency at the targeted implants compared to powering each implant separately. This was expected since the acoustic energy was split between two foci and a perfect superposition was not possible due to pulser quantization. The partitioned array suffered from increased beamwidth due to the reduced aperture of each sub-array, resulting in 0.33x and 0.21x efficiency at each implant. The results from simultaneous time reversal focusing on two implants at different depths (3 and 4 cm) is shown in Table 4.1. Superposition performed better than the partitioned array.
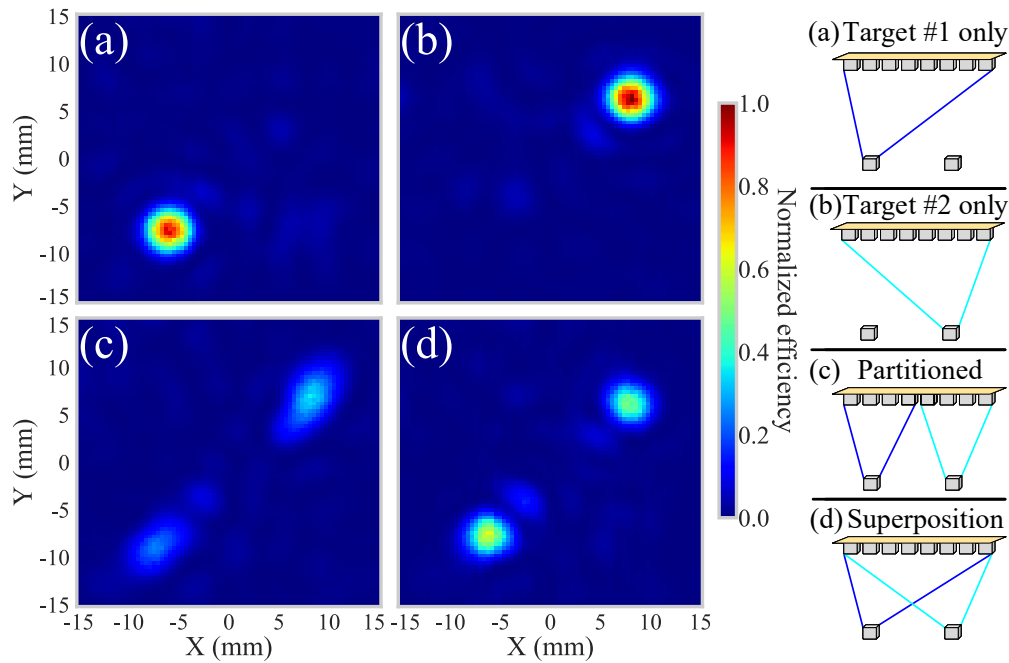
Figure 4.4: Energy transfer efficiency (normalized) with two implants at 5 cm depth with separate and simultaneous time reversal. Illustrations demonstrating each setup are also shown. (a) Target #1 (-6 mm, -8 mm) only. (b) Target #2 (8 mm, 6 mm) only. (c) Partitioned array. (d) Superposition.

Table 4.1: Efficiency (normalized to peak value) of separate and simultaneous time reversal measurements to 2 implants at different depths.

	Depth	Target 1	Target 2	Partitioned	Superposition
Implant 1	3 cm	1.0	0.009	0.34	0.41
Implant 2	4 cm	0.005	0.48	0.14	0.20

Chapter 5

Iterative time reversal

5.1 Backscatter modulation signal

The iterative reversal technique described in the introduction requires that the strongest set of received echos originate from the face of piezo itself. Other reflectors in tissue, particularly bone, can create stronger reflections. Even if the implant provides the strongest backscattered signal, the piezo is not the only component of the implant, since it also includes an integrated circuit and may include a capacitor. The flex-PCB substrate can also contribute significantly to these echos and result in a defocused beam after time reversal iterations. This is demonstrated in Fig. 5.1, which shows a cross-section of the acoustic field intensity after active drive time reversal and after iterative time reversal focusing. In this testing setup, the piezo was mounted on a long flex-PCB strip, which resulted in focusing along the length of the flex-PCB. While an assembled implant has a much smaller PCB substrate, this could still result in defocusing from the piezo target.

To achieve contrast with the surroundings during implant localization, [11] utilizes the 3rd harmonic produced by the rectifier connected to the piezo while [32] opens and shorts the piezo while sweeping the focus of the array during ultrasound B-mode imaging. Here, we use a related approach to the latter in order to identify the reflected signal originating solely from the piezo itself rather than its packaging or surroundings.

The backscatter received by a single array element after sending an unfocused ultrasound pulse is shown in Fig. 5.2(a), both with the implant piezo terminals open and shorted. The implant piezo is located at a depth of 50 mm and approximately 20° from the axis. In both conditions, the received waveform is composed of multiple reflections and it is not possible to isolate the reflection from the piezo face. However, taking the difference between the waveforms, i.e. the backscatter modulation between the two states, allows for isolation of the clean waveform in Fig. 5.2(b) which is known to originate from the piezo itself. Using this calculated waveform as the input for the time reversal or phase reversal procedure thus allows for reliable focusing on the piezo.

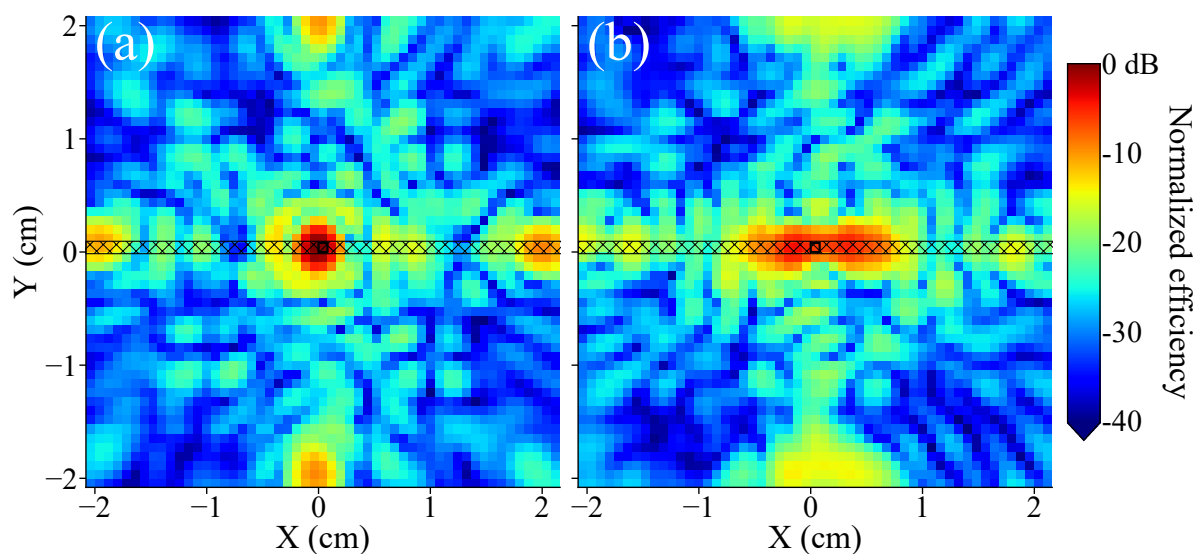Figure 5.1: Energy transfer efficiency using (a) active drive time reversal and (b) iterative time reversal showing defocusing from piezo resulting from flex-PCB. The location of the piezo target is shown by a black square and its flex-PCB substrate is the hatched rectangle.
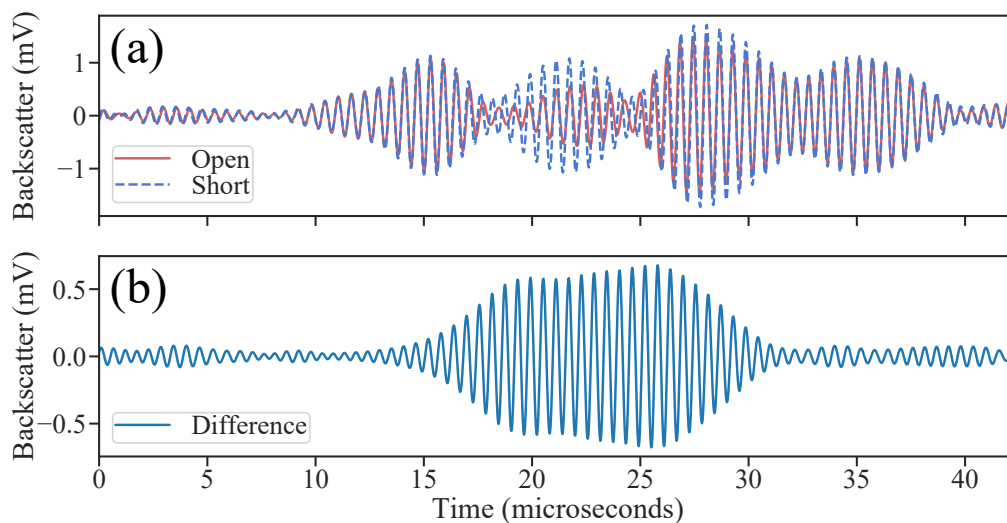

Figure 5.2: (a) Received backscatter on an array element with implant piezo open and shorted. (b) Difference between open and shorted signals

Using the calculated backscatter modulation as the signal for reversal also presents a method for targeting multiple implants separately or simultaneously. One limitation of the typical iterative time reversal procedure using the raw echos is that it will converge on the brightest, primary reflector. If multiple implants are present, then only the one which produces the strongest signal will be targeted. While a method has previously been developed to target weaker reflectors [33], using the backscatter modulation presents a simpler approach. By sending a command to a single implant to change its modulation state, the delays required to transmit to only that implant can be determined. This can be performed for each implant, allowing each implant to be targeted individually. As was demonstrated in [1], superposition of multiple signals can also be used to target multiple implants simultaneously, even with the low resolution of the US pulsers used.

5.2   Phase reversal procedure

Since the signals used here for time reversal contain the majority of their spectral power at a single frequency, the waveforms received can be reduced to amplitude and phase information. With the 3-level (-V_{High}, 0, +V_{High}) US pulsers and approximately sinusoidal waveforms, the outputs will either cycle between the three levels in an ON state or remain at 0 during an OFF state. During quantization, the received signal amplitude is used to determine whether the channel will be ON or OFF at a given time, but the higher resolution amplitude information is lost. This results in quantization error between the ideal time reversed pulse and the actual transmitted pulse. Finite element model simulations (COMSOL Multiphysics) showed a 10% efficiency improvement was possible using 9-level ($\approx$ 3-bit) quantization when focusing at 0° in a homogeneous medium. A previous study experimentally evaluating the effect of "one-bit time reversal" in a highly scattering medium observed good performance even after removal of the higher resolution amplitude information [34].

If no amplitude information is used, then the "reversed" waveforms can be constructed simply by applying a reversed delay to each array element based on measuring the relative delays between received signals. This was demonstrated through simulation in [12] and experimentally in [1], and this technique will be referred to as "phase reversal." An advantage of this approach compared to full time reversal is that it is possible to deliver pulses of arbitrary length to the implant, rather than relying on the length of the initial pulse.

When calculating the relative delays between the signals received on each element, an element near the array center is used as a reference. The maximum of the cross-correlation is found between this reference signal and the signals on each element to determine relative delays. However, this can result in in 2π offsets between elements, or "phase gaps" [33] For an infinitely long pulse, these 2π offsets will have no effect, but for shorter pulses it can be helpful to adjust these offsets so that the ultrasound waves produced by each element arrive at the implant at the same time. Therefore, an iterative process is used to shift element delays by increments of 2π if they differ substantially from neighboring elements. Fig. 5.3(a) shows
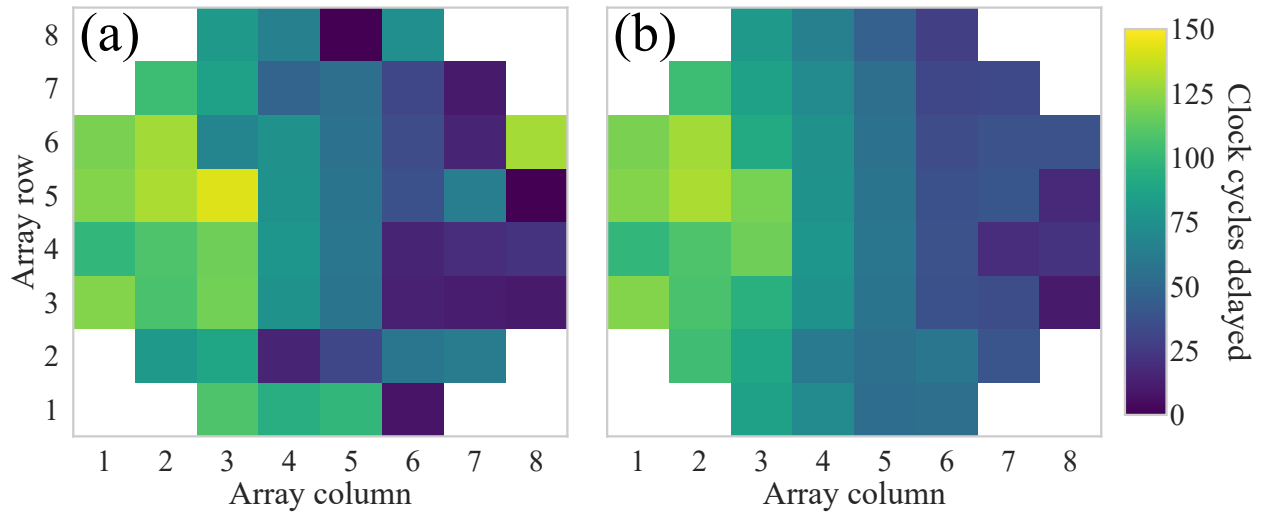
Figure 5.3: Example of relative delays (in 40 MHz clock cycles) determined (a) By finding the maximum of cross-correlation between received signals and (b) After adjustment by 2π shifts.

an example of the delays across the array calculated directly from the cross-correlations, while Fig. 5.3(b) shows the final delays after the adjustment procedure is applied.

5.3   Methods

The results in this chapter were obtained using the 2nd generation ultrasound system. In iterative pulse-echo mode, the drive voltage of the ultrasound array automatically varies from ± 25 V to ± 5 V depending on the amplitude of the received backscatter. This increases SNR when the implant is not aligned with the array while keeping the received echos within the range of the ADC when the implant is aligned. However, all measurements are taken with the drive voltage of the ultrasound array at ± 5 V. For iterative reversal, the array first sends out an unfocused ultrasound pulse. Using the difference signal corresponding to the backscatter modulation originating from the implant piezo, the system performs time or phase reversal. This process repeats until the transmitted ultrasound has converged on the target implant. The position of the 0.8 mm cube "implant" piezo in the oil medium is controlled by motorized translation stages (Thorlabs MTS50), and its open-circuit voltage is recorded using an oscilloscope and differential probe (Keysight N2750A). While operation at the series or parallel resonant frequencies is possible, the results shown were obtained while operating at the parallel resonant frequency of 1.7 MHz. While the implant piezo has a higher impedance at its parallel resonant frequency, it also has a higher open-circuit voltage, and this can result in a better volumetric efficiency when operating at parallel resonance [7].

As with the active drive reversal, the transmitted energy from the array is calculated from applied voltage waveforms, and the energy received by the implant is calculated from the received voltage waveform. Energy transfer efficiency is found by dividing received energy by transmitted energy.

5.4   Results

Efficiency through oil medium

Iterative time and phase reversal are compared to active uplink time and phase reversal in Fig. 5.4. Measurements were taken at a constant depth of 50 mm while sweeping the implant piezo along one direction of the array. As a comparison, results with time delay beamforming using the known implant location and without beamforming are also shown. Efficiency drops off at larger steering angles due to increased beamwidth, increased angular misalignment of the implant relative to the array, and additional attenuation from greater propagation distance.

Iterative time reversal was 4% more efficient, on average, than active uplink time reversal. Iterative phase reversal was also 4% more efficient, on average, than active uplink phase reversal. It was expected that both active uplink and iterative would result in the same efficiency or that active uplink would perform better; the cause of the slight improvement using iterative reversal is currently unknown. Use of full time reversal resulted in 5-10% better efficiency than its phase reversal approximation both in active uplink and iterative modes. All four methods were more efficient than time delay beamforming using the known implant position. Since the oil medium was homogenous and not highly scattering, this difference can likely be attributed to the fact that time delay beamforming did not account for irregularities in array geometry or implant angular misalignment. While this advantage may not be present if using a conventional ultrasound imaging array, this self-correction would be useful if the phased array was designed as part of a flexible, wearable device for which the exact array curvature may vary. All methods improved efficiency compared to the unfocused array by 1-2 orders of magnitude.
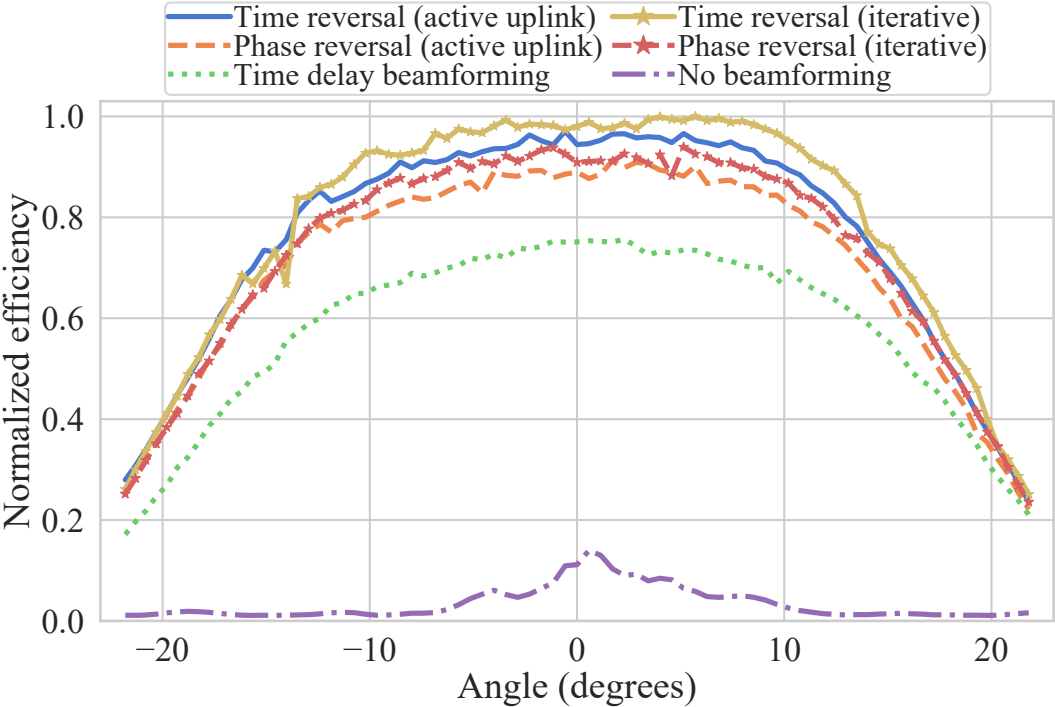
Figure 5.4: Efficiency vs beamforming angle (normalized to peak time reversal measurement) when focusing at each position using active uplink and iterative reversal methods, at 50 mm in oil.

Efficiency through tissue

Energy transfer efficiency was also evaluated when focusing through 2.5 cm of porcine tissue suspended in the oil medium at a total depth of 5 cm. These results are shown in Fig. 5.5, and are normalized to the same peak time reversal value measured with the oil medium in Fig. 5.4. Efficiency is lower through tissue due to greater attenuation in tissue and reflections at the oil-tissue interfaces. Iterative phase reversal again performs comparably to active uplink phase reversal, but the efficiency is highly dependent on local tissue properties. Iterative time reversal can also be performed through tissue, but that data was not obtained in time for this publication.
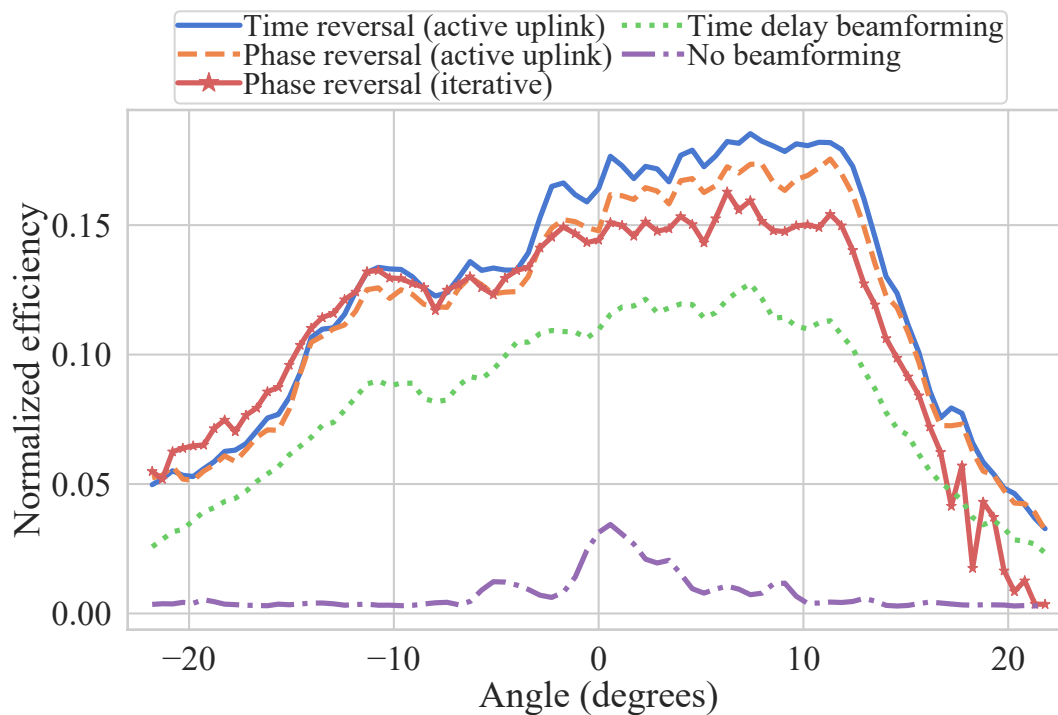

Figure 5.5: Efficiency vs beamforming angle when focusing at each position using iterative phase reversal and active uplink time/phase reversal, through oil and 2.5 cm tissue. Efficiency is normalized to the same value as in Fig. 5.4.

Iterations to convergence

Iterative reversal may require one or more iterations depending on the strength of the backscattered signals, as shown in Fig. 5.6. If the initial echo is strong, as is the case when the implant is already centered on the array, only one iteration is required. When the implant is off-center, more iterations are required. Still, convergence is achieved in only a few iterations, which improves the feasibility of tracking a moving implant in real-time.
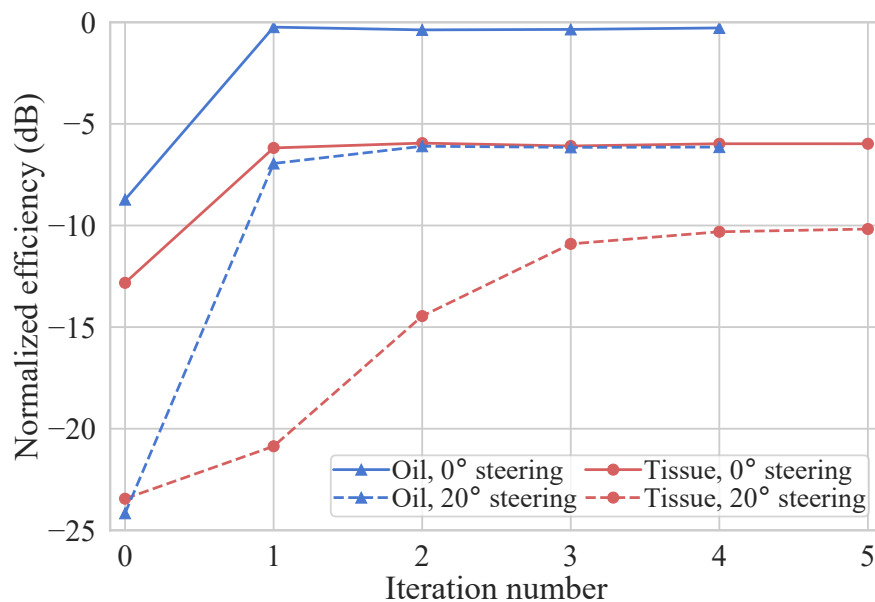

Figure 5.6: Efficiency over multiple iterations showing iterations to convergence under varying conditions.

Chapter 6

Discussion

In this work, we proposed and demonstrated the use of time reversal beamforming for ultrasound power delivery to millimeter or sub-millimeter sized implants. We showed how this could be used both in an active uplink mode if the implant communicates by actively driving its piezo and in an iterative pulse-echo mode if the implant communicates through passive backscattering. Time reversal and the related phase reversal approach both showed showed significantly better energy transfer efficiency than time delay beamforming using the known implant location. We showed that superposition could be used to simultaneously power two ultrasonic implants, and this was observed to be up to twice as efficient as using half the array to power each implant. Extending this approach to a greater number of simultaneous implants may further degrade efficiency, but implants could also be targeted sequentially.

Use of the backscatter modulation signal provides a method for locating and powering multiple implants with iterative time reversal. In future work this straightforward approach will be compared to a previously published method in which weaker reflectors can be targeted by subtracting the previously recorded echos from stronger reflectors [33]. Recently, we taped out an ultra low-power recording implant with a time-division multiplexing communication protocol that will allow the external transducer to program and receive data from multiple implants. With a few modifications, these "DustNet" devices could be programmed to alternately short and open their piezos during the startup sequence to allow for robust iterative time reversal beamforming.

While we implemented time reversal beamforming using a custom planar phased array and ultrasound system, this method can be used with any 1D or 2D ultrasound array. It could also be used with a sparse random array, in which the irregular position of elements prevents the production of grating lobes while requiring relatively few channels [35]. However, typical ultrasound phased array systems for imaging or high intensity focused ultrasound therapy are not suitable for extended or wearable applications due to their form factor and reliance on gel for acoustic coupling to tissue.

Consider the control of a prosthetic arm using a network of implants located along the

remaining peripheral nerves of an amputee. Since the external transducer will be attached to part of an arm in motion, it must be able to correct for the changing alignment between itself and the implants, and ideally it will also allow for implants to be located on multiple nerves. This necessitates the use of a planar phased array to allow for steering of ultrasound power within the 3D tissue volume. However, using a 2D planar array results in quadratically increasing channel count compared to a 1D linear array. The system size is already limited due to the wearable nature of the device, so the design of the array must be carefully considered to maximize total power delivered to the implant while meeting FDA guidelines for diagnostic ultrasound. Our analysis has shown that an array with a pitch greater than the typical $\lambda/2$ allows for maximizing power at the target without sacrificing efficiency.

While most ultrasound arrays require gel for acoustic coupling, this is not ideal for long-term applications. A flexible or stretchable array could conform to the skin without the need for gel, as has recently been demonstrated [36]. Due to the power-limited environment of a wearable device and the desire to dissipate the minimum amount of acoustic energy in tissue while powering chronic implants, beamforming efficiency should be maximized. Time reversal provides a theoretically optimal approach to beamforming and accounts for tissue inhomogeneity and changing geometry of a flexible/stretchable array. The eventual development of a compact phased array system with simple on-chip processing for time reversal beamforming would greatly improve the feasibility of powering a network of miniaturized implants for neural recording and stimulation.

References

[1] B. C. Benedict, M. M. Ghanbari, S. F. Alarnouti, N. T. Ersumo, and R. Muller, "Time reversal beamforming for powering ultrasonic implants," in *2021 10th International IEEE/EMBS Conference on Neural Engineering (NER)*, 2021, pp. 647–650. DOI: `10.1109/NER49283.2021.9441162`.

[2] D. K. Piech, B. C. Johnson, K. Shen, M. M. Ghanbari, K. Y. Li, R. M. Neely, J. E. Kay, J. M. Carmena, M. M. Maharbiz, and R. Muller, "A wireless millimetre-scale implantable neural stimulator with ultrasonically powered bidirectional communication," *Nature Biomedical Engineering*, vol. 4, no. 2, pp. 207–222, 2020.

[3] J. Charthad, T. C. Chang, Z. Liu, A. Sawaby, M. J. Weber, S. Baker, F. Gore, S. A. Felt, and A. Arbabian, "A mm-sized wireless implantable device for electrical stimulation of peripheral nerves," *IEEE Transactions on Biomedical Circuits and Systems*, vol. 12, no. 2, pp. 257–270, 2018. DOI: `10.1109/TBCAS.2018.2799623`.

[4] J. Thimot and K. Shepard, "Bioelectronic devices: Wirelessly powered implants," *Nature Biomedical Engineering*, vol. 1, p. 0051, Mar. 2017. DOI: `10.1038/s41551-017-0051`.

[5] M. J. Weber, Y. Yoshihara, A. Sawaby, J. Charthad, T. C. Chang, and A. Arbabian, "A miniaturized single-transducer implantable pressure sensor with time-multiplexed ultrasonic data and power links," *IEEE Journal of Solid-State Circuits*, vol. 53, no. 4, pp. 1089–1101, 2018. DOI: `10.1109/JSSC.2017.2782086`.

[6] M. Ghanbari, D. Piech, K. Shen, S. Alamouti, C. Yalcin, B. Johnson, J. Carmena, M. Maharbiz, and R. Muller, "A sub-mm³ ultrasonic free-floating implant for multi-mote neural recording," *IEEE Journal of Solid-State Circuits*, vol. PP, pp. 1–14, Sep. 2019. DOI: `10.1109/JSSC.2019.2936303`.

[7] M. M. Ghanbari and R. Muller, "Optimizing volumetric efficiency and backscatter communication in biosensing ultrasonic implants," *IEEE Transactions on Biomedical Circuits and Systems*, pp. 1–1, 2020. DOI: `10.1109/TBCAS.2020.3033488`.

[8] H. S. Gougheri, A. Dangi, S.-R. Kothapalli, and M. Kiani, "A comprehensive study of ultrasound transducer characteristics in microscopic ultrasound neuromodulation," *IEEE Transactions on Biomedical Circuits and Systems*, vol. 13, no. 5, pp. 835–847, 2019. DOI: `10.1109/TBCAS.2019.2922027`.

[9] D. Seo, H. Tang, J. M. Carmena, J. M. Rabaey, E. Alon, B. E. Boser, and M. M. Maharbiz, "Ultrasonic beamforming system for interrogating multiple implantable sensors," in *2015 37th Annual International Conference of the IEEE Engineering in Medicine and Biology Society (EMBC)*, 2015, pp. 2673–2676. DOI: `10.1109/EMBC.2015.7318942`.

[10] M. L. Wang, T. C. Chang, T. Teisberg, M. J. Weber, J. Charthad, and A. Arbabian, "Closed-loop ultrasonic power and communication with multiple miniaturized active implantable medical devices," in *2017 IEEE International Ultrasonics Symposium*, 2017, pp. 1–4.

[11] M. L. Wang, T. C. Chang, and A. Arbabian, "Ultrasonic implant localization for wireless power transfer: Active uplink and harmonic backscatter," in *2019 IEEE International Ultrasonics Symposium (IUS)*, 2019, pp. 818–821. DOI: `10.1109/ULTSYM.2019.8926006`.

[12] M. Meng and M. Kiani, "Self-image-guided ultrasonic wireless power transmission to millimeter-sized biomedical implants," in *2019 41st Annual International Conference of the IEEE Engineering in Medicine and Biology Society (EMBC)*, 2019, pp. 364–367. DOI: `10.1109/EMBC.2019.8857559`.

[13] M. Fink, "Time reversal of ultrasonic fields. i. basic principles," *IEEE transactions on ultrasonics, ferroelectrics, and frequency control*, vol. 39, pp. 555–66, Feb. 1992. DOI: `10.1109/58.156174`.

[14] M. Fink, G. Montaldo, and M. Tanter, "Time-reversal acoustics in biomedical engineering," *Annual Review of Biomedical Engineering*, vol. 5, no. 1, pp. 465–497, 2003. DOI: `10.1146/annurev.bioeng.5.040202.121630`.

[15] D. Arnaud, P. Roux, and M. Fink, "Robust acoustic time reversal with high-order multiple scattering," *Physical review letters*, vol. 75, pp. 4206–4209, Jan. 1996. DOI: `10.1103/PhysRevLett.75.4206`.

[16] R. J. Mailloux, *Phased Array Antenna Handbook*, 2nd ed. Boston: Artech House, 2005.

[17] S.-C. Wooh and Y. Shi, "Optimum beam steering of linear phased arrays," *Wave Motion*, vol. 29, pp. 245–265, Apr. 1999. DOI: `10.1016/S0165-2125(98)00039-0`.

[18] G. S. Kino, *Acoustic Waves: Devices, Imaging, and Analog Signal Processing*. Englewood Cliffs, N.J: Prentice Hall, Jan. 1987, ISBN: 978-0-13-003047-4.

[19] T. L. Szabo, *Diagnostic Ultrasound Imaging: Inside Out*, 2nd edition. Amsterdam ; Boston: Academic Press, Dec. 2013, ISBN: 978-0-12-396487-8.

[20] J. Jensen and N. Svendsen, "Calculation of pressure fields from arbitrarily shaped, apodized, and excited ultrasound transducers," *IEEE Transactions on Ultrasonics, Ferroelectrics, and Frequency Control*, vol. 39, no. 2, pp. 262–267, 1992. DOI: `10.1109/58.139123`.

[21] J. A. Jensen, "Field: A program for simulating ultrasound systems," in *10TH Nordibaltic Conference on Biomedical Imaging*, 1996, pp. 351–353.

[22] F. a. D. Administration, *Marketing Clearance of Diagnostic Ultrasound Systems and Transducers*, Jun. 2019. [Online]. Available: `https://www.fda.gov/media/71100/download`.

[23] S. Sonmezoglu, J. R. Fineman, E. Maltepe, and M. M. Maharbiz, "Monitoring deep-tissue oxygenation with a millimeter-scale ultrasonic implant," *Nature Biotechnology*, vol. 39, no. 7, pp. 855–864, Jul. 2021, ISSN: 1546-1696. DOI: `10.1038/s41587-021-00866-y`.

[24] S. F. Alamouti, M. M. Ghanbari, N. T. Ersumo, and R. Muller, "High throughput ultrasonic multi-implant readout using a machine-learning assisted cdma receiver," in *2020 42nd Annual International Conference of the IEEE Engineering in Medicine Biology Society (EMBC)*, 2020, pp. 3289–3292. DOI: `10.1109/EMBC44109.2020.9176480`.

[25] H. Azhari, *Basics of Biomedical Ultrasound for Engineers*. John Wiley & Sons, Mar. 2010, ISBN: 978-0-470-56146-1.

[26] H. W. Johnson and M. Graham, *High-speed Digital Design: A Handbook of Black Magic*. Prentice Hall, 1993, ISBN: 978-0-13-395724-2.

[27] V. T. Rathod, "A review of electric impedance matching techniques for piezoelectric sensors, actuators and transducers," *Electronics*, vol. 8, no. 2, 2019, ISSN: 2079-9292. DOI: `10.3390/electronics8020169`.

[28] *OPA355 data sheet, product information and support — TI.com*. [Online]. Available: `https://www.ti.com/product/OPA355` (visited on 08/02/2021).

[29] *OPA846 data sheet, product information and support — TI.com*. [Online]. Available: `https://www.ti.com/product/OPA846#tech-docs` (visited on 07/28/2021).

[30] *AFE5804 data sheet, product information and support — TI.com*. [Online]. Available: `https://www.ti.com/product/AFE5804` (visited on 08/12/2021).

[31] T. C. Chang, M. Wang, and A. Arbabian, "Multi-access networking with wireless ultrasound-powered implants," in *2019 IEEE Biomedical Circuits and Systems Conference (BioCAS)*, IEEE, 2019, pp. 1–4.

[32] Y. Zhang and K. L. Shepard, "A 0.6-mm2 powering and data telemetry system compatible with ultrasound b-mode imaging for freely moving biomedical sensor systems," in *2019 IEEE Custom Integrated Circuits Conference (CICC)*, 2019, pp. 1–4. DOI: `10.1109/CICC.2019.8780205`.

[33] G. Montaldo, M. Tanter, and M. Fink, "Revisiting iterative time reversal processing: Application to detection of multiple targets," *The Journal of the Acoustical Society of America*, vol. 115, no. 2, pp. 776–784, Feb. 2004, ISSN: 0001-4966. DOI: `10.1121/1.1636463`.

[34] A. Derode, A. Tourin, and M. Fink, "Ultrasonic pulse compression with one-bit time reversal through multiple scattering," *Journal of Applied Physics*, vol. 85, no. 9, pp. 6343–6352, May 1999, ISSN: 0021-8979. DOI: 10.1063/1.370136.

[35] S. Goss, L. Frizzell, J. Kouzmanoff, J. Barich, and J. Yang, "Sparse random ultrasound phased array for focal surgery," *IEEE Transactions on Ultrasonics, Ferroelectrics, and Frequency Control*, vol. 43, no. 6, pp. 1111–1121, 1996. DOI: 10.1109/58.542054.

[36] C. Wang, B. Qi, M. Lin, Z. Zhang, M. Makihata, B. Liu, S. Zhou, Y.-h. Huang, H. Hu, Y. Gu, Y. Chen, Y. Lei, T. Lee, S. Chien, K.-I. Jang, E. B. Kistler, and S. Xu, "Continuous monitoring of deep-tissue haemodynamics with stretchable ultrasonic phased arrays," *Nature Biomedical Engineering*, vol. 5, no. 7, pp. 749–758, Jul. 2021, ISSN: 2157-846X. DOI: 10.1038/s41551-021-00763-4.